Science Advances
AAAS

Supplementary Materials for

Strong suppression of heat conduction in a laboratory replica of galaxy-cluster turbulent plasmas

Jena Meinecke, Petros Tzeferacos, James S. Ross, Archie F. A. Bott, Scott Feister, Hye-Sook Park, Anthony R. Bell, Roger Blandford, Richard L. Berger, Robert Bingham, Alexis Casner, Laura E. Chen, John Foster, Dustin H. Froula, Clement Goyon, Daniel Kalantar, Michel Koenig, Brandon Lahmann, Chikang Li, Yingchao Lu, Charlotte A. J. Palmer, Richard D. Petrasso, Hannah Poole, Bruce Remington, Brian Reville, Adam Reyes, Alexandra Rigby, Dongsu Ryu, George Swadling, Alex Zylstra, Francesco Miniati, Subir Sarkar, Alexander A. Schekochihin, Donald Q. Lamb, Gianluca Gregori*

*Corresponding author. Email: gianluca.gregori@physics.ox.ac.uk

Published 9 March 2022, *Sci. Adv.* **8**, eabj6799 (2022)
DOI: 10.1126/sciadv.abj6799

This PDF file includes:

SUPPLEMENTARY INFORMATION

CALCULATION OF PLASMA PARAMETERS

The plasma was generated from the ablation of plastic foil targets (CH), manufactured by General Atomics, with trace amounts of homogeneously distributed dopants, listed in Table I. Due to the composition of the doped targets, the effective ion charge seen by the free electrons was calculated for a multi-species plasma as follows:

$$Z_{\rm eff} = \frac{1}{n_{\rm e}} \sum_j Z_j^2 n_j, \tag{1}$$

where the indices j refer to each target element. From the quasineutrality condition, it follows that the electron density can be expressed as $n_{\rm e} = \sum_j Z_j n_j$. To simplify these equations, we can relate the density of each elemental component to that of hydrogen by setting $n_j = R_{j\rm H} n_{\rm H}$, where $R_{j\rm H}$ is the ratio of a given element's concentration to the amount of hydrogen in each sample foil, e.g., $R_{\rm OH} = 1.2/49.6$. This reduces the effective ion charge equation to

$$Z_{\rm eff} = \frac{\sum_j R_{j\rm H} Z_j^2}{\sum_j R_{j\rm H} Z_j} \tag{2}$$

for j = H, C, O, N, Mn, Co, and $R_{\rm HH} = 1$. To determine the effective ion charge as seen by the hydrogen atoms, Equation (2) is modified as $Z_{\rm eff,B} = [(\sum_j R_{j\rm H} Z_j^2) - Z_{\rm H}^2] / \sum_j R_{j\rm H} Z_j$.

Figure 3 in the main text shows a line-integrated electron temperature map over the 2 × 1 mm^2 interaction region. From the histogram of the temperature distribution, the mean value corresponds to $T_{\rm e} = T_{\rm i} = 1.1$ keV, as shown in Table I (assuming local thermodynamic equilibrium). The value at 10% of the peak is $T_{\rm e} = T_{\rm i} = 1.6$ keV.

The inflow and turbulent velocities were both measured directly with the time-resolved stimulated Brillouin scattering (SBS) diagnostic. The SBS diagnostic collected reflected light from four, frequency-tripled laser probe beams, collectively delivering 5.7 kJ of energy in a 12.6 ns picket pulse with a 150 μm spot size. Two of the SBS beams were pointed offset from the target chamber center (TCC), at 500 μm towards each of the foils, to measure the inflow velocity, determined from the start of the SBS signal. A third SBS beam, pointed at TCC, was used to determine the turbulent velocity, as discussed in the main text.

Quantity	**Experimental Value**
Composition of target	48.3% C, 49.6% H, 1.2% O, 0.6% N, 0.1% Mn, 0.1% Co
Average atomic weight ($\langle M \rangle$)	6.7
Mean ion charge ($\langle Z \rangle$)	3.6
Effective ion charge ($Z_{\rm eff}$)	5.7
Hydrogen effective ion charge ($Z_{\rm eff,B}$)	5.5
Electron temperature ($T_{\rm e}$)	1100 eV
Ion temperature ($T_{\rm i}$)	1100 eV
Electron number density ($n_{\rm e}$)	4.9×10^{20} cm^{-3}
Turbulent velocity ($v_{\rm turb}$)	2×10^7 cm s^{-1}
Outer scale (L)	0.06 cm
RMS magnetic field ($B_{\rm RMS}$)	0.8 MG
Maximum magnetic field ($B_{\rm max}$)	3.0 MG
Adiabatic index ($\gamma_{\rm I}$)	5/3

Supplementary Table I. Summary of target characteristics and direct experimental measurements of plasma parameters at t = 25 ns after the start of the drive laser pulse. The outer scale, L, represents the distance between two neighboring grid aperture centers. Values are reported in CGS, except for the temperature that is given in eV.

Using the experimental values in Table I, we calculated the relevant plasma parameters indicated in Table II. Both the hydrogen-ion and electron-ion mean free paths are smaller than the system size ($L \approx 0.06$ cm), $\lambda_{\mathrm{Hion}}, \lambda_{\mathrm{e}} = 0.0013$ cm $\ll L$.

Quantity	**Formula**	**Value**
Coulomb logarithm ($\log\Lambda$)	$23.5 - \log n_{\mathrm{e}}^{1/2} T_{\mathrm{e}}^{-5/4} - \sqrt{10^{-5} + \frac{(\log T_{\mathrm{e}} - 2)^2}{16}}$	7.2
Mass density (ρ)	$1.7 \times 10^{-24} (\sum_j M_j n_j)$	1.6×10^{-3} g cm^{-3}
Debye length (λ_{D})	$7.4 \times 10^2 \frac{T_{\mathrm{e}}^{1/2}}{n_{\mathrm{e}}^{1/2}} \left[1 + \frac{T_{\mathrm{e}}}{T_{\mathrm{i}}} Z_{\mathrm{eff}}\right]^{-1/2}$	4.2×10^{-7} cm
Sound speed (c_{s})	$9.8 \times 10^5 \frac{[(\langle Z \rangle + 1)\gamma_{\mathrm{I}} T_{\mathrm{e}}]^{1/2}}{\langle M \rangle^{1/2}}$	3.5×10^7 cm s^{-1}
Mach number	$\mathrm{v}_{\mathrm{turb}}/c_{\mathrm{s}}$	0.6
Plasma β	$4.0 \times 10^{-11} \frac{n_{\mathrm{e}} T_{\mathrm{e}} + \sum_j n_j T_{\mathrm{i}}}{B_{\mathrm{RMS}}^2}$	44
H-ion mean free path (λ_{Hion})	$2.1 \times 10^{13} \frac{T_{\mathrm{i}}^2}{\left(Z_{\mathrm{H}}^2 Z_{\mathrm{eff,B}} n_{\mathrm{e}} \log\Lambda\right)}$	1.3×10^{-3} cm
Electron-ion mean free path (λ_{e})	$2.1 \times 10^{13} \frac{T_{\mathrm{e}}^2}{\left(Z_{\mathrm{eff}} n_{\mathrm{e}} \log\Lambda\right)}$	1.2×10^{-3} cm
Electron Larmor radius (r_{g})	$2.4 \frac{T_{\mathrm{e}}^{1/2}}{B_{\mathrm{RMS}}}$	1.0×10^{-4} cm
Hydrogen Larmor radius (ρ_{H})	$1.0 \times 10^2 \frac{M_{\mathrm{H}}^{1/2} T_{\mathrm{i}}^{1/2}}{Z_{\mathrm{H}} B_{\mathrm{RMS}}}$	4.1×10^{-3} cm
Unmagnetized thermal diffusivity (χ_{S})	$3.0 \times 10^{21} \frac{T_{\mathrm{e}}^{5/2}}{Z_{\mathrm{eff}} n_{\mathrm{e}} \log\Lambda}$	5.9×10^6 cm^2 s^{-1}
Magnetized thermal diffusivity (χ_{m})	$\chi_{\mathrm{S}} r_{\mathrm{g}}/\lambda_{\mathrm{e}}$	4.7×10^5 cm^2 s^{-1}
Suppressed thermal diffusivity (χ)	$\sim\chi_{\mathrm{S}}/150$	3.9×10^4 cm^2 s^{-1}
Turbulent Péclet number ($\mathrm{Pe}_{\mathrm{turb}}$)	$\mathrm{v}_{\mathrm{turb}} L/\chi$	$\sim$30
Dynamic viscosity (μ)	$4.27 \times 10^{-5} \frac{M_{\mathrm{H}}^{1/2} T_{\mathrm{i}}^{5/2} n_{\mathrm{H}}}{\log\Lambda Z_{\mathrm{eff,B}} n_{\mathrm{e}}}$	7 g cm^{-1} s^{-1}
Kinematic viscosity (ν)	μ/ρ	4.3×10^3 cm^2 s^{-1}
Turbulent Reynolds number ($\mathrm{Re}_{\mathrm{turb}}$)	$\mathrm{v}_{\mathrm{turb}} L/\nu$	280
Viscous dissipation scale (l_ν)	$L/\mathrm{Re}_{\mathrm{turb}}^{3/4}$	8.8×10^{-4} cm
In-flow Resistivity ($\eta_{\|\|}$)	$3.1 \times 10^5 \frac{Z_{\mathrm{eff}} \log\Lambda}{T_{\mathrm{e}}^{3/2}}$	350 cm^2 s^{-1}
Magnetic Reynolds number ($\mathrm{Rm}_{\mathrm{turb}}$)	$\mathrm{v}_{\mathrm{turb}} L/\eta_{\|\|}$	3.5×10^3
Magnetic Prandtl number (Pm)	Rm / Re	12
Resistive dissipation scale (l_η)	$L/\mathrm{Pm}^{1/2}$	2.5×10^{-4} cm

Supplementary Table II. Summary of derived plasma parameters at t = 25 ns after the start of the drive laser pulse. The values are reported in CGS.

GATED X-RAY DETECTOR TO DIAGNOSE ELECTRON TEMPERATURES

Here we introduce a passive diagnostic configured to measure spatially-resolved electron temperature profiles using a gated X-ray detector (GXD), which includes an X-ray framing camera, differential filtering, a pinhole array, and two sets of collimator arrays.

The GXD was mounted onto a diagnostic snout to diagnose a side profile of the plasma flows as illustrated in Figure 1 of the main text. The GXD was equipped with two sets of collimator arrays, both of which comprised of a staggered array of four collimators, 250 µm in diameter. A pinhole array comprising a staggered array of four pinholes, 25 μm in diameter, was positioned between the two sets of collimator arrays, at a distance that enabled a 2× magnification of the interaction region. Each of the four pinholes were concentrically aligned to each respective collimator of both collimator arrays and staggered to avoid overlap of images onto 4-strips of the X-ray framing camera. All four of the strips were independently timed to enable the temporal characterization of the plasma. At least two of the pinholes were equipped with distinct filters to uniquely attenuate the X-ray plasma emission associated with each pinhole at a similar time (e.g., t = 25 ns as illustrated in Figure 2 of the main text) before imaging onto the camera. In the absence of an absolute calibration of the X-ray framing camera, a direct comparison of the uniquely-attenuated X-ray plasma emission from the two pinholes enabled a characterization of the electron temperature. The distinct filters were positioned on a kinematic base, in front of the camera. For most shots, 6.56 μm of polyimide (Poly) covered half of the camera and two of the staggered pinholes, each of them independently timed with gate width of 100 ps. The second half of the camera was covered with 2.38 μm of vanadium (V) to filter the remaining two pinholes, which were co-timed with first two. For each shot we therefore collected four X-ray images: two Poly-filtered images taken at two distinct times, and two V-filtered images co-timed with the Poly-filtered images. Based on the magnification of the GXD, the expected spatial resolution of the X-ray images is 50 μm. We also note that for a turbulent velocity of 2×10^7 cm s^{-1}, the blurring induced by the turbulent motions within the gate width of the camera is 20 μm.

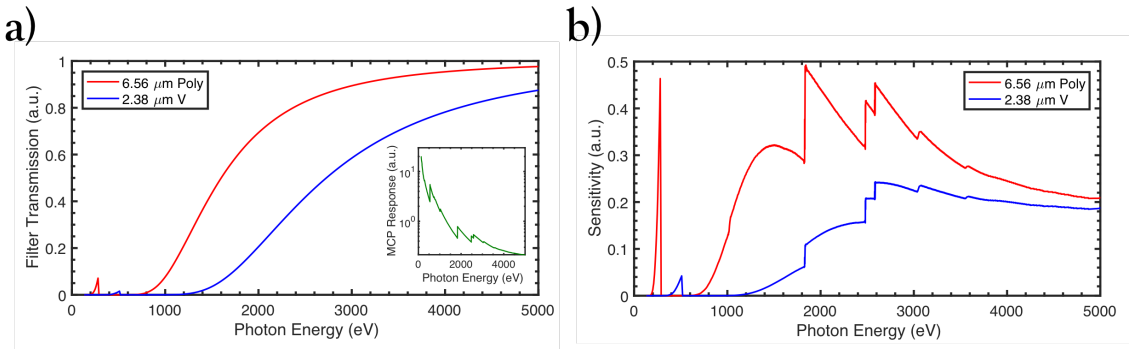

FIG. S1. **X-ray detector's response.** **(a)** Filter transmission curves, with reference to the Center for X-Ray Optics at Lawrence Berkeley National Laboratory database, for 6.56 μm thick polyimide (Poly) and 2.38 μm thick vanadium (V) used in experimental shots. The inset shows the relative microchannel plate (MCP) response of the NIF X-ray framing cameras [31]. **(b)** Sensitivity curves for each filter, determined by comparing each transmission curve to the MCP response shown in (a).

The sensitivity curves of the GXD diagnostic take into account both the relative MCP response of the camera and the filter transmission of each filter chosen for a particular shot. In Figure S1b, the sensitivity was calculated by multiplying the filter transmission with the MCP response for each discrete photon energy. We specifically chose filters (i.e., Poly and V) that were both compatible with the facility requirements and had significantly different transmission curves.

We modeled the X-ray spectrum emitted from a region of given density (between 10^{19} and 10^{21} cm^{-3}) and temperature (in the range 200–5000 eV) using SPECT3D (www.prism-cs.com). SPECT3D is a collisional-radiative spectral analysis code designed to simulate the atomic and radiative properties of laboratory and astrophysical plasmas. Given the multi-component nature of the plasma, we used PrOpacEOS (Prism opacity and equation of state code) equation of state tables, with non-LTE atomic transitions to generate simulated X-ray spectra, an example of which is shown in Figure S2a.

For many different combinations of electron temperatures and densities, the synthetic X-ray spectra were used to determine expected frequency-resolved signal of each filter. In the example of Figure S2b, an expected frequency-resolved signal for each filter was calculated by multiplying a simulated X-ray spectrum for $T_e = 900$ eV and $n_e = 10^{20}$ cm^{-3} with each respective sensitivity (shown in Figure S1b). A ratio of the two signals was calculated and plotted as a discrete point of the curves in Figure S3. This process was repeated for numerous combinations of electron

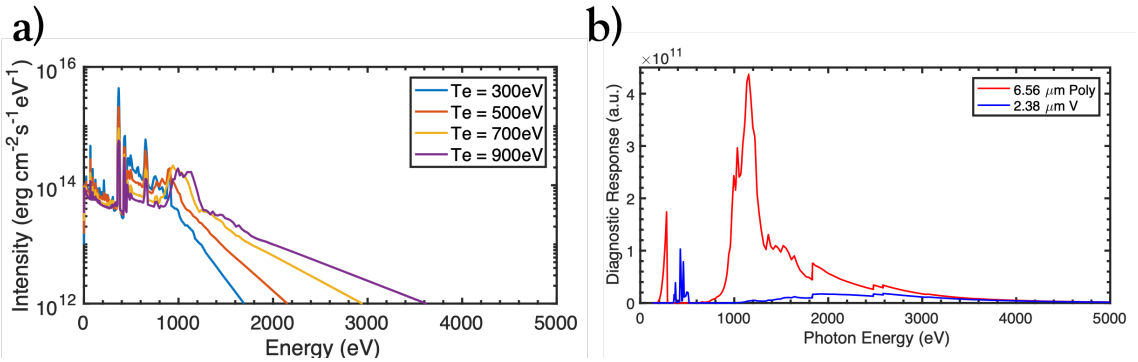

FIG. S2. **Plasma emission spectra.** **(a)** SPECT3D calculated X-ray spectra, assuming an electron density of 10^{20} cm^{-3}. **(b)** Expected frequency-resolved signal measured by the GXD diagnostic for $T_e = 900$ eV and $n_e = 10^{20}$ cm^{-3}.

temperatures and densities to calculate the ratio curves in Figure S3. The latter relate the electron temperature of the plasma with a ratio of the X-ray plasma emission collected by the GXD for each filter (i.e., a ratio of Poly-filtered emission to V-filtered emission), for a fixed density. Note that opacity effects can be neglected and the emission is optically thin for all plasma conditions considered here.

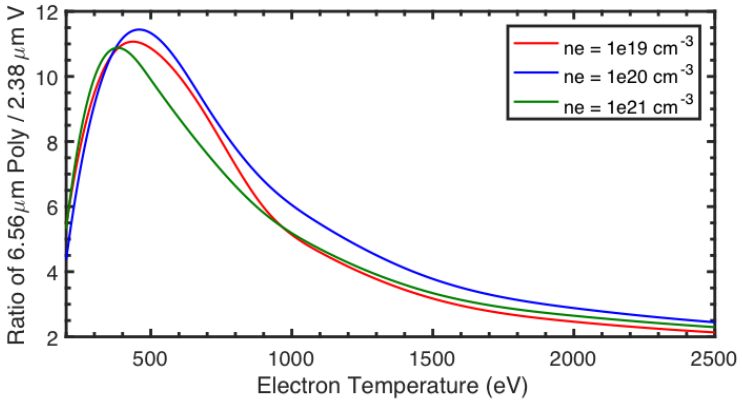

FIG. S3. **X-ray ratio curves to extract the electron temperature measure from the data.** The ratio curves of 6.56 μm polyimide and 2.38 μm vanadium are displayed for different electron densities.

From Figure S3, we first note that the shape of the curves is rather insensitive to the electron density, and mostly depends on the electron temperature. Moreover, the choice of filters results in a peak in the ratio curve near $T_e \sim$450 eV. If we exclude temperatures below 450 eV on the basis that the plasma is expected to be much hotter (as indicated by FLASH simulations), then there is a one-to-one correspondence between the measured emission ratio and the plasma's electron temperature. Therefore, in a plasma with uniform density and temperature, the value of the filter ratio can be use to infer an electron temperature. For $T_e > 2.5$ keV, the ratio curve becomes flat with temperature, thus determining the upper sensitivity bound.

For a plasma with spatially varying emission – which itself arises directly from variations in temperature and density – an interpretation of the two-dimensional temperature maps recovered using our technique is required. In the special case when the emission predominantly arises from a volume in the plasma with only small variations in density and temperature with respect to some mean value, a reasonable interpretation for the maps is that of the electron temperature, mass-averaged along the line of sight. On the other hand, if there are large departures from the mean value of temperature (and particularly if those values surpass the reported sensitivity bounds), this interpretation becomes more complex. We verify both of these claims using the 3D FLASH simulations of our experiment described in the next section.

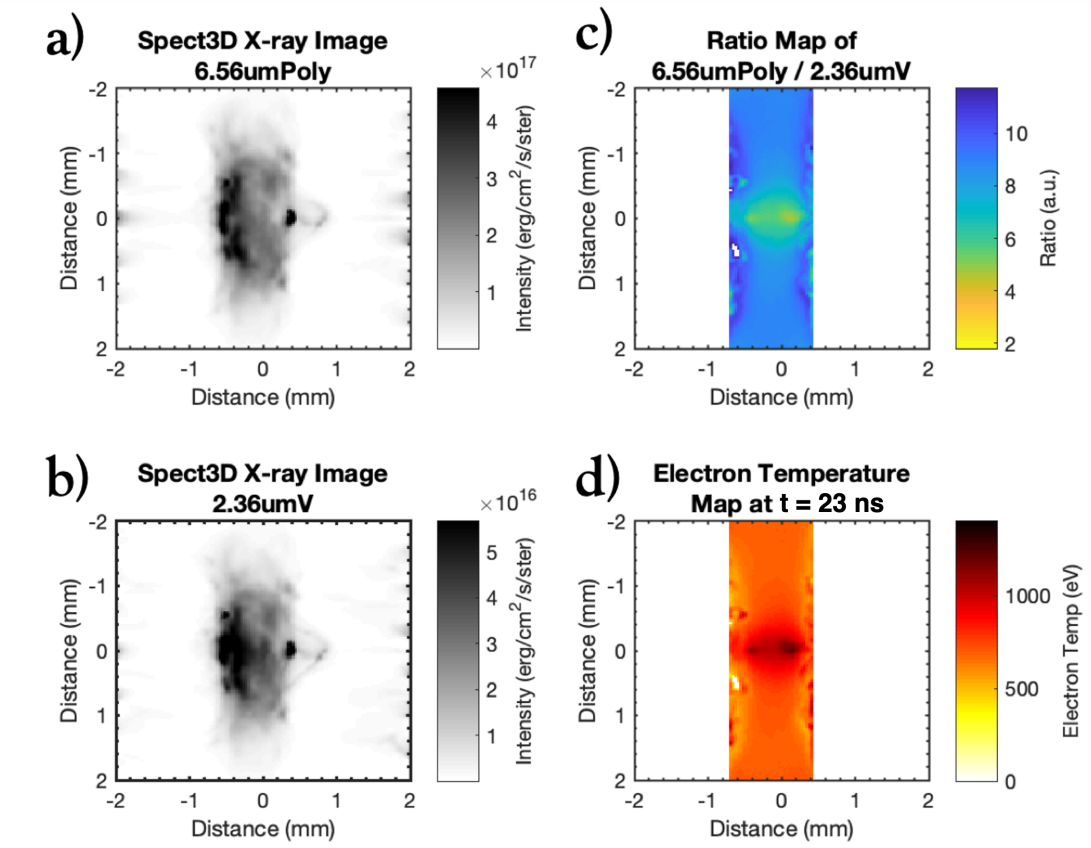

FIG. S4. **Validation of the electron-temperature measure.** **(a)** and **(b)** show 2-D synthetic X-ray images from the conduction-on FLASH simulations, accounting for the two different filter transmissions. The intensity ratio map is shown in **(c)**. The ratio map has been calculated by ignoring data outside the central interaction region (that is, points with horizontal coordinate lower than -1 mm and larger than 1 mm have been ignored). **(d)** The electron temperature is extracted from the X-ray intensity ratio as shown in Figure S3.

Interpretation of temperature measurements

We used simulations carried out with the FLASH code to design, execute, and interpret the experiments discussed here. While the FLASH simulations are described in detail in a companion paper, here we discuss how they were used to interpret the temperature measurements derived from the GXD. FLASH [32] is a publicly available, parallel, multi-physics, adaptive mesh refinement (AMR), finite-volume Eulerian [33] hydrodynamics and magneto-hydrodynamics (MHD) code developed at the Flash Center for Computational Science. FLASH scales well to over a 100,000 processors, and uses a variety of parallelization techniques including domain decomposition, mesh replication, and threading to optimally utilize hardware resources. FLASH is professionally managed software with version control, coding standards, extensive documentation, user support, and integration of code contributions from external users. The code is subject to daily, automated regression testing on a variety of platforms. Over the past nine years, extensive High Energy Density Physics (HEDP) and extended-MHD capabilities have been added in FLASH [34] as part of the U.S. DOE NNSA-funded FLASH HEDP Initiative and through support by Los Alamos National Laboratory (LANL) and Lawrence Livermore National Laboratory (LLNL). These include multiple state-of-the art hydrodynamic and MHD shock-capturing solvers; a generalized Ohm's law that incorporates extended MHD terms of the Braginskii formulation [35]; three-temperature extensions with anisotropic thermal conduction, heat exchange, multigroup radiation diffusion, tabulated multi-material equations of state and opacities, laser energy deposition, and numerous simulated diagnostics [21]. The FLASH code and its capabilities have been validated through benchmarks and code-to-code comparisons [36, 37], as well as through direct application to laboratory experiments [19–21, 34, 38–47]. The latter include experiments carried out at the Omega Laser Facility that employed the TDYNO (turbulent dynamo) platform used in this work [19, 20, 46]. For a discussion on the evolution of the platform, see Ref. [48].

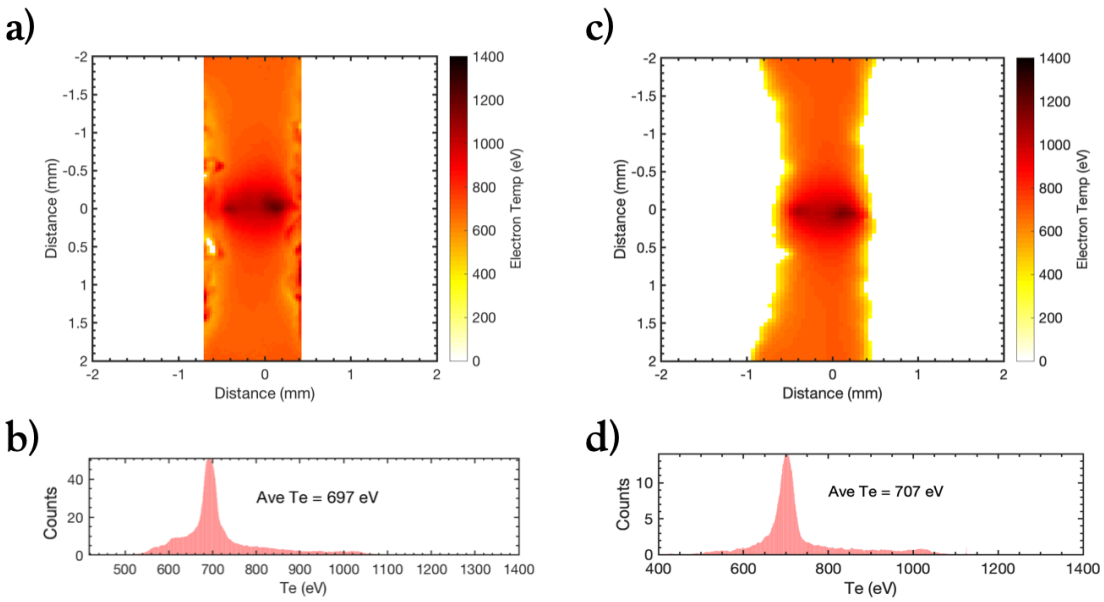

FIG. S5. **Comparison between synthetic electron-temperature measure and mass-averaged temperature maps.** **(a)** Extracted temperature profiles from the synthetic X-ray images' intensity ratio, assuming a constant electron density $n_e = 5.5 \times 10^{20}$ cm^{-3}. **(b)** Corresponding temperature distributions for panel **(a)**. **(c)** Mass-averaged temperatures, along the GXD detector line of sight, obtained from FLASH simulations at $t = 25$ ns. **(d)** Corresponding temperature distributions for panel **(c)**.

Conduction-on case. To interpret the temperature measurements, we first consider conduction-on FLASH simulations (i.e., with the inclusion of Spitzer conductivity in the system of equations evolved by FLASH [34]), which exhibit smooth interaction-region temperature profiles with small fluctuations with respect to the mean value. We post-processed the results of these simulations at $t = 23$ ns with SPECT3D to produce a synthetic X-ray image of the interaction region as seen by the GXD diagnostics. SPECT3D was run with various filters in front of the detector. The resultant images are shown in Figure S4, with a 50 μm spatial smoothing applied to mimic the instrument resolution. As we did with the experimental images, we first create a map of X-ray intensity ratios, and then, taking $n_e = 5.5 \times 10^{20}$ cm^{-3} (as measured at this time with optical Thomson scattering), construct an electron-temperature map.

The comparison between the inferred GXD temperature map from the synthetic X-ray images and the temperature map obtained by mass averaging the electron temperature (from FLASH simulations) along the same line of sight is shown in Figure S5. The two images are, indeed, remarkably similar, giving us confidence in the diagnostic approach. We observe an average temperature of 648 eV and a peak temperature of ~ 1 keV with the synthetic GXD diagnostics. From the FLASH simulations, we obtain a mass-averaged temperature of 697 eV with a peak of ~ 1.1 keV, which is almost identical to the previous values. Furthermore, the temperature distributions in the two images are quantitatively very similar, as shown in Figures S5b and S5d.

The differences between the GXD calculated temperature and the mass-averaged FLASH temperatures are mainly attributed on the assumption of constant density in the GXD retrieval, as illustrated in Figure S3. On average, the estimated error associated with this assumption is $< 10\%$. This can be seen in Figure S6. By assuming a lower value for the density, $n_e = 2.8 \times 10^{20}$ cm^{-3} (that is, 50% lower than before), we can achieve an even more accurate electron-temperature map. A comparison between this GXD predicted map and the FLASH temperatures produces an error in the central interaction region that is $< 5\%$ (see Figure S6c).

Finally, instead of using an average electron density for the whole region, we can assume a different (line-of-sight averaged) electron density for each position along the map. Taking these averaged densities from FLASH simulations and retrieving the electron temperature from the synthetic X-ray intensity ratios, we arrive at the map shown in Figure S7. This shows marginal further improvement over the previous estimates, again reinforcing the point that the analysis developed here seems rather robust with respect to the particular value of electron density in the plasma.

Error analysis. With our temperature diagnostics having been validated using synthetic data, we look now at the measured data and attempt to provide a full error analysis. When dealing with the experimental data, we need to account for a few additional manipulations compared to what we did with the simulations. First, to each measured

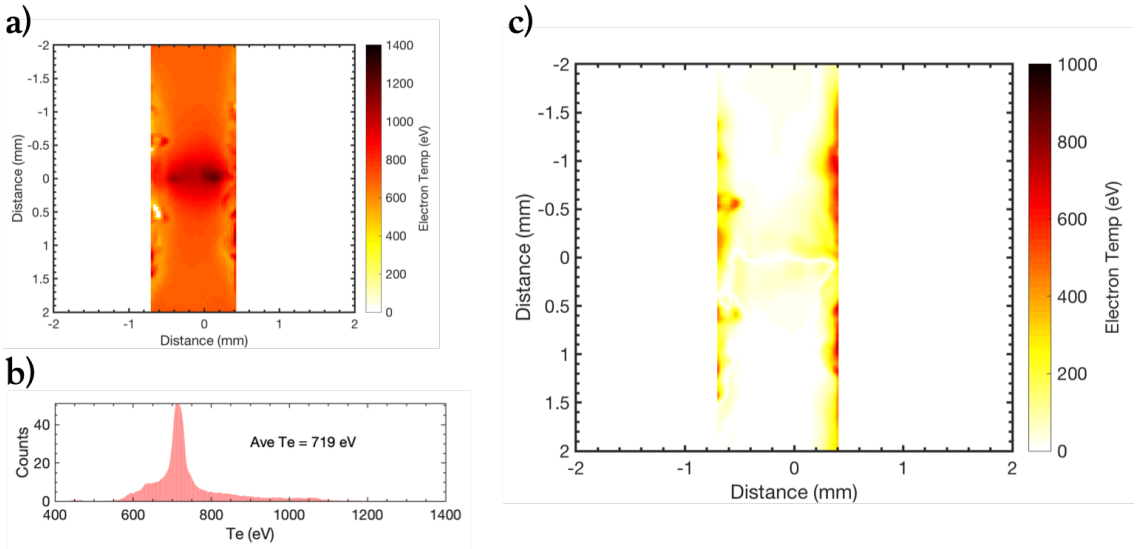

FIG. S6. **Further comparisons with fixed densities.** **(a)** Same as in Figure S5a but assuming $n_e = 2.8 \times 10^{20}$ cm^{-3}. **(b)** Temperature distributions corresponding to the map shown in panel **(a)**. **(c)** Absolute temperature difference between panel **(a)** and Figure S5a.

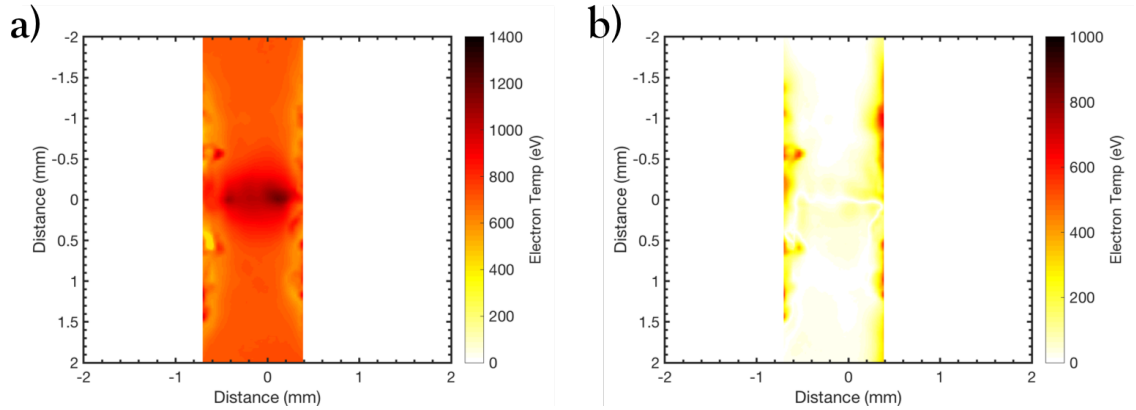

FIG. S7. **Further comparisons with spatially varying densities.** **(a)** Same as in Figure S5c but taking the FLASH averaged density along the line of sight at each position. **(b)** Absolute temperature difference between panel **(a)** and Figure S5a.

X-ray image we apply a background subtraction. Secondly, while the GXD snout had a nominal 25 μm diameter pinhole array, we have to account for possible variations (of order of $10\% - 20\%$) in their size.

Errors in the filter thickness must also be taken into consideration (they can be as high as 20%, according to the filters' manufacturer). In Figure S8a we plot the X-ray intensity ratio, assuming variations in the filters' thickness. We see clearly that the range of intensity ratios can vary depending on the exact thickness of the filters. While this would normally be a problem, we were able to deduce the actual filter thickness from the data itself. Plotted in Figure S8b is the distribution of X-ray intensity ratios in the interaction region at two different times. This plot shows a range of values from 2.2 to 12. Assuming that the filter thickness does not vary significantly in space, we then look at the available ratio curves and determine which of the curves in Figure S8a best reproduces this range.

In the main text, we compare temperature maps obtained on NIF to those recorded on the Omega laser facility. The GXD diagnostic is identical for the two experiments, with the only difference being that the Omega filter combination was 2 μm mylar plus 40 nm Al and 4 μm mylar plus 80 nm Al, and the ratio curve was obtained assuming the average electron density $n_e = 10^{19}$ cm^{-3}.

Conduction-off case. Next, we perform the same analysis on the conduction-off FLASH simulations (i.e., with the omission of Spitzer conductivity, switched off immediately prior to the formation of the turbulent interaction

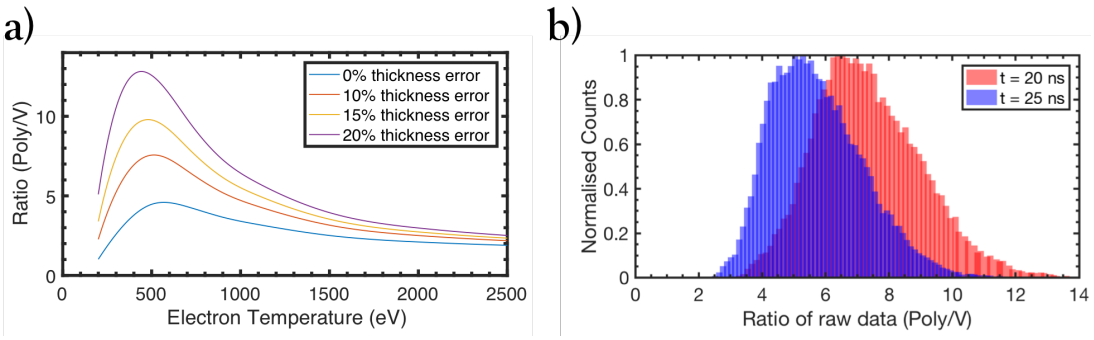

FIG. S8. **Error analysis in the ratio curves. (a)** Calculated intensity-ratio curves assuming errors in the nominal filter thickness (the filters' manufacturer, GoodFellow, advises that a ±20% error in the supplied materials should be accounted for). **(b)** Intensity histograms for the NIF measurements at two different times. We note ratio values ranging from $2.2 - 12$. Such a range can only be obtained assuming 18% error in the filter thickness. This selects the ratio curve used in the data analysis.

region) at $t = 23$ ns: we produce 2-D synthetic X-ray images using SPECT3D with the appropriate filters, take the ratio, and infer a map of the electron-temperature measure $\langle T_e \rangle_X$ (see Figure S9a). This can again be compared with the electron temperature mass-averaged along the line of sight, $\langle T_e \rangle_{\rm mass}$, determined directly from the simulations (Figure S9b). Qualitatively, the maps remain similar, but quantitatively there is some discrepancy, particularly in the area corresponding to the central fiducial volume discussed in the main text; quantitative agreement is better in the wings of the interaction-region plasma. These findings can be illustrated using a pointwise scatter plot that compares $\langle T_e \rangle_X$ with $\langle T_e \rangle_{\rm mass}$ (Figure S9c) for both the center of the interaction-region plasma, and its wings. While the scatter points in the wings cluster close to the line $\langle T_e \rangle_{\rm mass} \approx \langle T_e \rangle_X$, the clustering for points in the central volume is less strong. The most probable explanation for the discrepancy stems from the presence of large temperature fluctuations (and therefore density fluctuations, since the central region is in approximate pressure balance, as shown in the next subsection) in the conduction-off FLASH simulations. The volumes with intensity ratios below the sensitivity peak at ∼450 eV of the polyimide-vanadium filter configuration translate into electron-temperature measures $\langle T_e \rangle_{\rm X}$ above this value. For the central region, which has a slightly lower mean temperature than the wings, ∼20% of the overall volume has a temperature below the sensitivity peak as a result these fluctuations (Figure S9d), whereas the equivalent figure for the wings is only ∼5%.

We note that the electron temperature in the conduction-off FLASH simulations will be subject to a small amount of numerical diffusion, despite the absence of physical thermal conductivity. As a result, the effective Péclet number will not be infinite in the FLASH simulations. The latter were executed using a variant of the Piecewise Parabolic Method (PPM, [49]), with an explicit diffusive flux added to the numerical fluxes. The diffusion coefficient associated with the energy flux (viz. equation 4.2 in Ref. [49]) can therefore be used to provide an order-of-magnitude estimate of the effective numerical thermal diffusivity $\chi_{\rm n} \propto K \nabla \cdot \mathbf{v} \Delta^2$. Here K is a non-dimensional constant ($K = 0.1$ in the simulations), $\nabla \cdot \mathbf{v}$ is the multidimensional divergence of the velocity (viz. equation 4.5 in Ref. [49] and $\langle \nabla \cdot \mathbf{v} \rangle \sim 4 \times 10^7\,{\rm s}^{-1}$ in the interaction region), and Δ is the resolution element of the simulation ($\Delta \sim 25 \times 10^{-4}$ cm). This yields $\chi_{\rm n} \sim 25\,{\rm cm}^2\,{\rm s}^{-1} \ll \chi$, and a numerical Péclet number ${\rm Pe}_{\rm n} = {\rm v}_{\rm turb} L/\chi_{\rm n} = 4,800 \gg {\rm Pe}_{\rm turb}$.

Temperature measurements with copper-vanadium filter configuration

In addition to measuring spatially-resolved profiles of the line-of-sight-averaged electron temperature measure $\langle T_e \rangle_{\rm X}$ using the polyimide-vanadium filter configuration described in the main text, on a different shot day we performed similar measurements employing an alternative filter configuration: 0.8 μm of copper filtering two strips of the GXD camera, and 2.4 μm of vanadium filtering another two strips of the camera. X-ray images from this configuration at the two main times considered in the main text (23 ns and 25 ns after the initiation of the NIF drive beams) are shown in Figure S10. The images themselves are qualitatively similar to those reported in the main text (see Figures 1 and 2b), showing a region of strongly emitting plasma with localized fluctuations in that emission associated with turbulence. We note that the orientation of the GXD camera employed when collecting the data shown in Figure S10 was not identical, and so it is to be expected that the vanadium-filtered images shown in S10 are not identical to the analogous images given in the main text.

As with the polyimide-vanadium filter configuration, we infer maps of $\langle T_e \rangle_{\rm X}$ from the copper- and vanadium-filtered images by performing SPECT3D simulations to determine the X-ray emission detected using each filter from a uniform

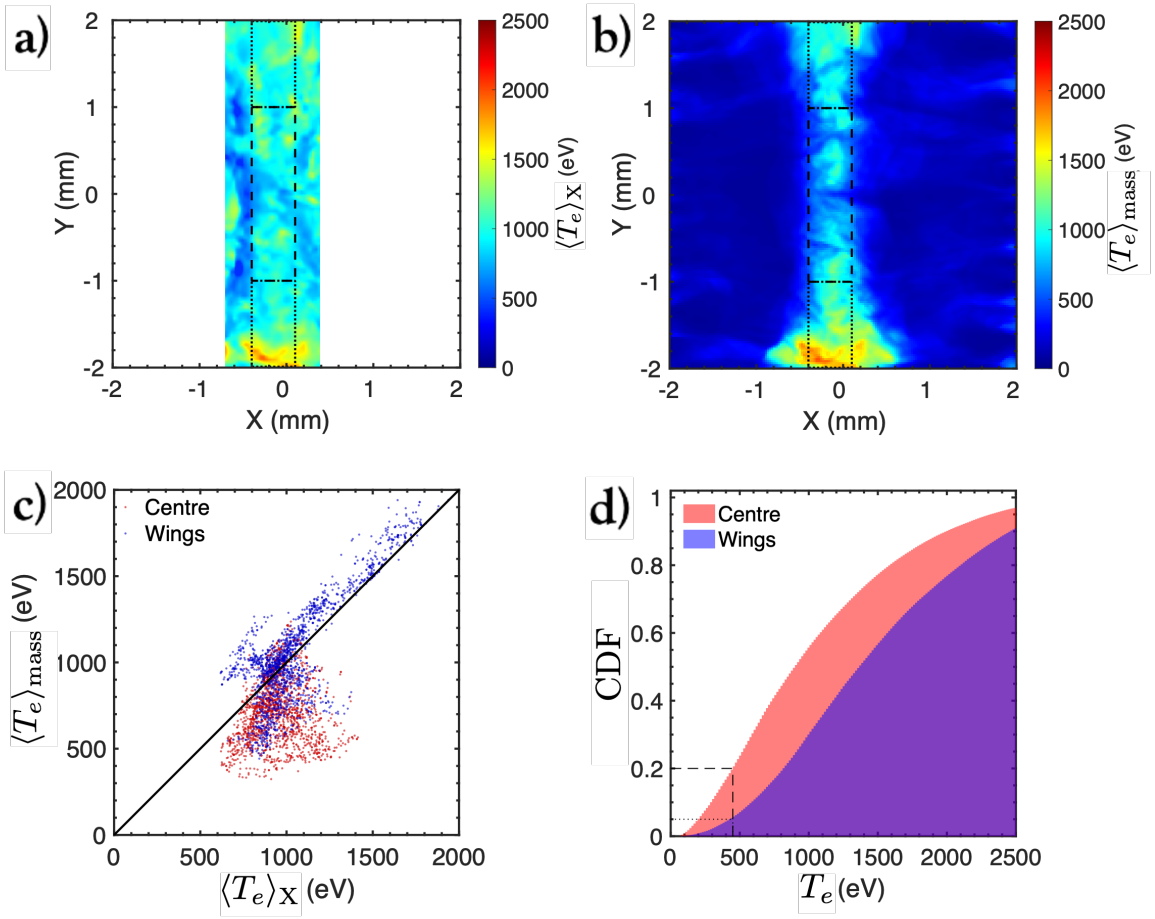

FIG. S9. **Interpretation of electron-temperature measure in presence of strong temperature fluctuations. (a)** 2D slice plot of the electron-temperature measure $\langle T_e \rangle_X$ derived from post-processed conduction-off FLASH simulations at $t = 23$ ns. The cross-section of the $2 \times 2 \times 0.4$ mm^3 'central' fiducial volume discussed in the main text is shown (dashed lines), along with the cross-section of two $2 \times 1 \times 0.4$ mm^3 'wing' fiducial volumes (dotted lines). **(b)** Same as (a), but for line-of-sight, mass-averaged temperature $\langle T_e \rangle_{\rm mass}$. **(c)** Scatter plot of $\langle T_e \rangle_X$ against $\langle T_e \rangle_{\rm mass}$ for all points in central and wing fiducial volumes. **(d)** Cumulative density function of the electron temperatures for the central and wing fiducial volumes. The dashed and dotted lines mark the fraction of the central and wing fiducial volumes, respectively, which are above the ∼450 eV peak of the temperature-ratio curve.

plasma with a known electron temperature (and density). We then (once again) derive a relation between the ratio of X-ray intensities and the electron temperature, and subsequently apply it to a ratio map that is determined directly from the measured X-ray data. Inferred maps of $\langle T_e \rangle_{\rm X}$ for the copper-vanadium filter combination taken at 23 ns and 25 ns are shown in Figures S11a and S11d, respectively. Qualitatively, the maps are similar to those shown in Figures 3a and 3b of the main text, with order-unity small-scale temperature fluctuations clearly evident. However, the maps are not quantitatively identical: the mean inferred value of $\langle T_e \rangle_{\rm X}$ is ∼20-30% lower than that inferred from the polyimide- and vanadium-filtered images.

To help interpret this modest difference, we also generated 2D synthetic temperature maps of the FLASH-simulated plasmas (both with and without conduction) using the copper-vanadium filter configuration at 23 ns (cf. Figure 3g and 3h of the main text, which show the equivalent maps generated with the polyimide-vanadium configuration). These maps are shown in Figures S11b and S11c, respectively. We find that, once again, the map of $\langle T_e \rangle_{\rm X}$ derived from the conduction-on FLASH simulation is qualitatively distinct to the map inferred from the experimental data, whereas the map inferred from the conduction-off simulation is much more similar. We also observe the same shift in the inferred mean value of $\langle T_e \rangle_{\rm X}$ towards lower values; the shift is therefore most plausibly interpreted as being a systematic error associated with application of the copper-vanadium filter configuration for the particular plasma conditions realized in our experiments. The origin of this systematic error can be further elucidated by comparing the ratio curves derived from SPECT3D simulations (see Figure S11e); the curve associated with the copper-vanadium

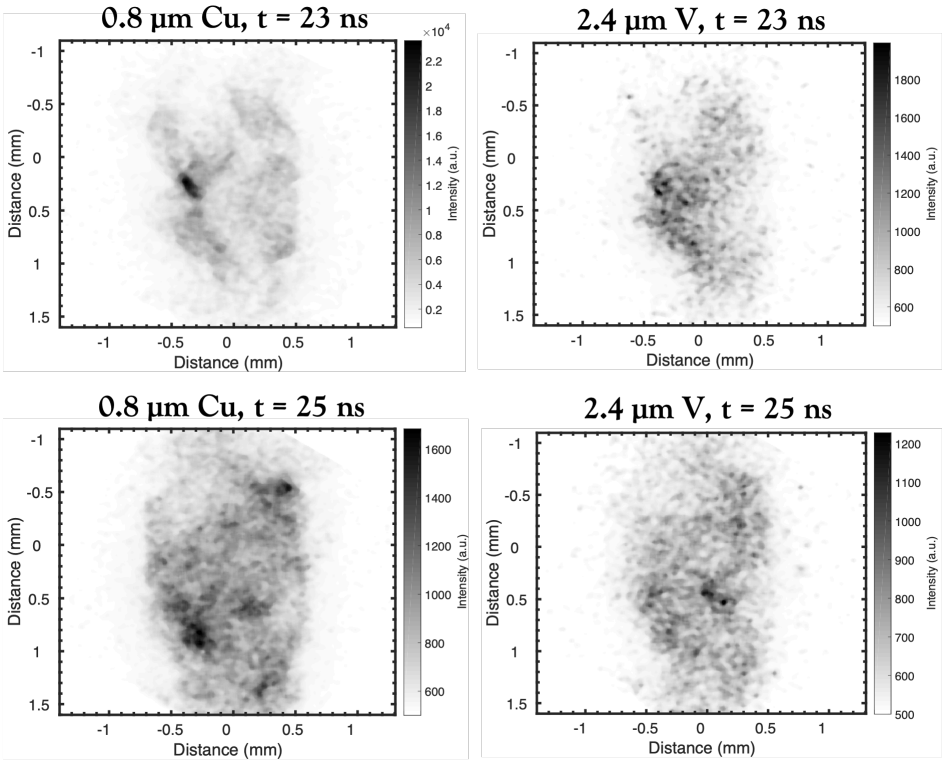

FIG. S10. **Measured X-ray data using a Cu/V filter combination.** Broadband X-ray emission from the turbulent interaction-region plasma imaged using the GXD camera and filtered with 0.8 μm copper (left column) and 2.4 μm vanadium (right column). The images on the top row are collected at 23 ns after the initial drive lasers fired, and the bottom row at 25 ns.

filter configuration is sensitive to a narrower range of temperatures (∼0.4-0.8 keV) than the polyamide-vanadium filter configuration (∼0.45-2 keV), with the mean value of the former interval being a factor ∼2 smaller. The consequences of these differences are evident in the map of $\langle T_e \rangle_X$ that we infer from the copper- and vanadium-filtered images collected at 25 ns (Figure S11d), which shows that in many places the signal lies below the detection threshold, and in a 1D temperature profile at this time (Figure S11f), which shows that the inferred values of $\langle T_e \rangle_X$ are restricted to a narrow band near the upper sensitivity bound, prohibiting the construction of a continuous temperature map. These results indicate that the copper-vanadium filter configuration is inferior to the polyimide-vanadium filter configuration for the particular plasma conditions realized in our experiments, and so we focus our analysis and discussion in the main text on the latter.

In short, the observation of significant temperature fluctuations (and thereby suppressed conduction) that we report in the main text – which is based on X-ray imaging data collected using the GXD camera configured with polyimide/vanadium filters – is supported by X-ray imaging data collected on other shots using the GXD camera configured with a different filter combination (as we state in the main text).

Pressure balance and radiative cooling in the conduction-off FLASH simulations

In the main text, we claim that the central part of the interaction-region plasma is in approximate pressure balance; here, we verify that this is indeed the case in the conduction-off FLASH simulations of our experiment. Figures S12a-c show 2-D plots of the electron number density, temperature and pressure in these simulations in the X-Y plane. It can be seen by eye that, in spite of all quantities varying across the central part of the interaction-region plasma, fluctuations in density and temperature have a significantly larger magnitude than the pressure (the large magnitude of electron temperature fluctuations in the interaction-region plasma is particularly evident in both 2D plots of this quantity in the Y-Z plane (Figure S12d), or profiles in the Z direction at fixed values of Y (Figure S12e)). More quantitatively, Figure S12f shows a pointwise scatter plot of electron number density and temperature. We see that the latter is inversely correlated with the former over an (order-of-magnitude) range of values, and is consistent with

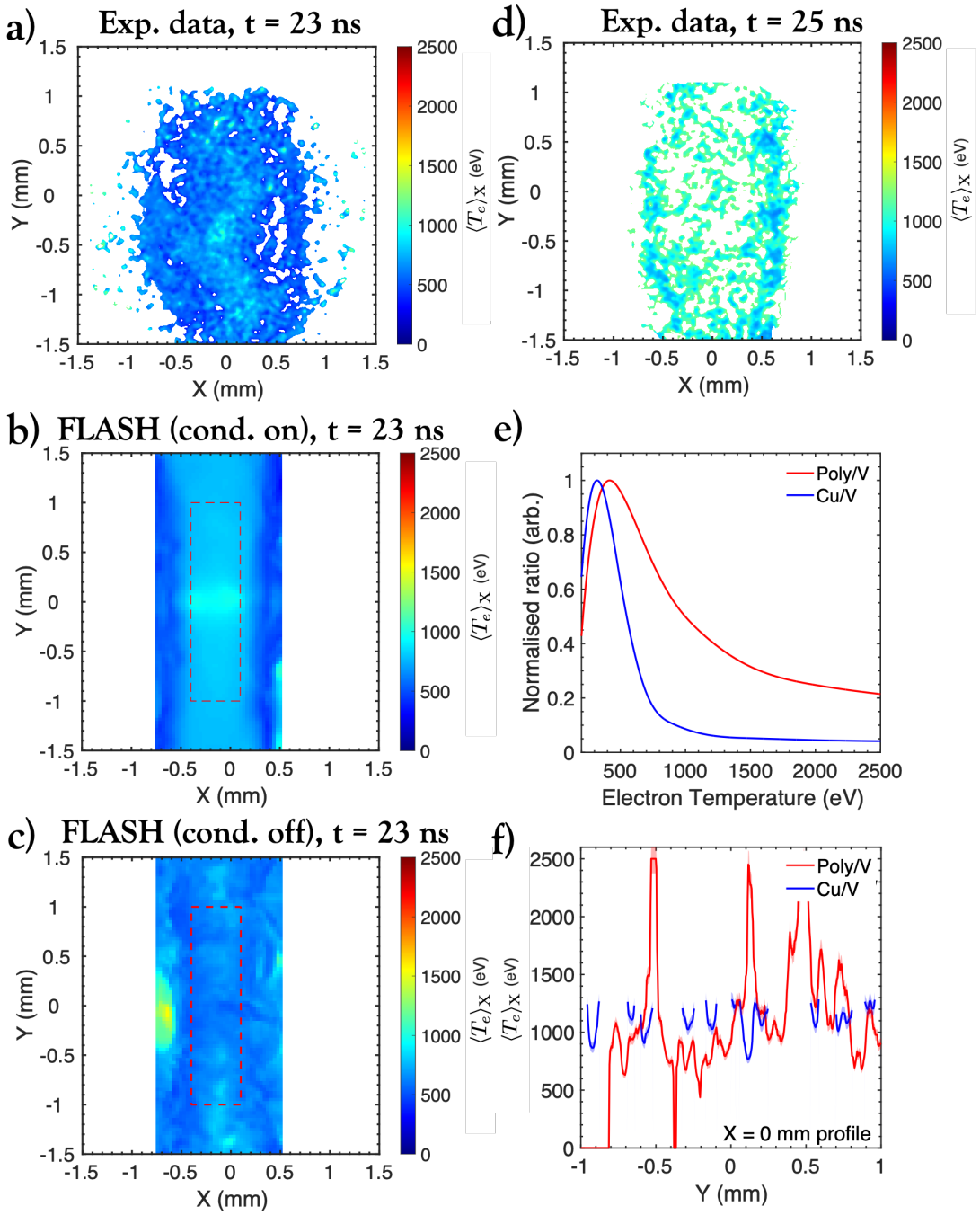

FIG. S11. **Electron-temperature measure maps from Cu/V filter combination.** **(a)**. Map of the line-of-sight-averaged electron-temperature measure $\langle T_e \rangle_X$ at $t = 23$ ns after the start of the NIF laser drive. The maps are derived from the X-ray intensity ratio using the copper-vanadium filter configuration (as opposed to the polyimide-vanadium filter configuration described in Figure 2d of the main text). **(b)** Synthetic temperature map constructed by post-processing FLASH simulation results of the NIF experiment (using the X-ray intensity ratio and GXD response of the copper-vanadium filter configuration) at $t = 23$ ns. The map shown in this panel was obtained for the case of Spitzer thermal conduction switched on. **(c)** Same as panel (b) but with Spitzer thermal conduction switched off. **(d)** Same as panel (a) but at $t = 25$ ns. **(e)** Comparison between the X-ray intensity ratio of the polyimide-vanadium filter configuration (red) and the copper-vanadium filter configuration (blue) to the electron temperature of the plasma. To aid comparison, the reported ratio curves are normalized to their maximum respective values. **(f)** Vertical temperature profiles taken at the $X = 0$ mm position for the temperature map in (d) derived from the copper-vanadium filter configuration, and the profile shown in Figure 3e of the main text (which was derived from the polyimide-vanadium filter configuration).

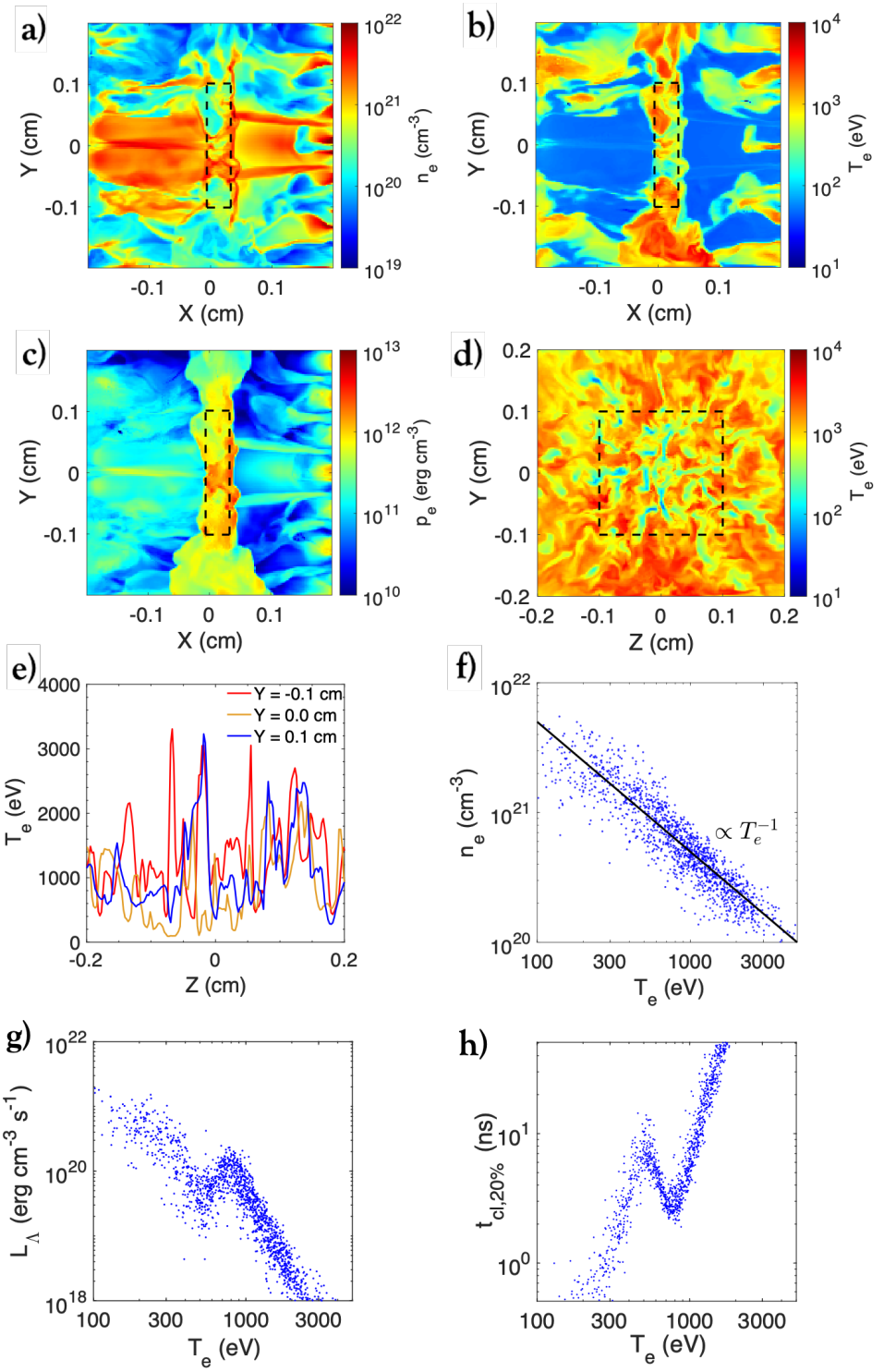

FIG. S12. **Post-processing of FLASH simulation results.** **(a)** 2D slice plot in the $Z = 0$ plane of the electron number density in the conduction-off FLASH simulation at $t = 23$ ns. The cross-sectional area of the $2 \times 2 \times 0.4$ mm^3 'central' fiducial volume discussed in the main text is shown. **(b)** Same as (a), but for electron temperature. **(c)** Same as (a), but for electron pressure. **(d)** 2D slice plot in the $X = 0$ plane of electron temperature in the conduction-off FLASH simulation at $t = 23$ ns. The cross-sectional area of the $2 \times 2 \times 0.4$ mm^3 'central' fiducial volume discussed in the main text is shown. **(e)** Temperature profiles (in the Z direction) in the $X = 0$ plane of electron temperature in the conduction-off FLASH simulation at $t = 23$ ns. **(f)** Scatter plot of the electron temperature against the electron number density at 1,500 random selected points from the conduction-off FLASH simulations in the central fiducial volume. **(g)** Same as f), but with scatter plot of the cooling function against electron temperature. **h)** Same as f), but with scatter plot of the estimated time taken for the plasma to cool 20% against electron temperature.

the ideal electron pressure p_e satisfying $p_e \propto n_e T_e \sim$ const., as claimed.

We also claim in the main text that radiative-cooling instabilities play a role in generating and sustaining the temperature fluctuations in the interaction-region plasma. We support this claim here by calculating the cooling function L_Λ in the conduction-off FLASH simulations, and then computing a pointwise scatter plot of L_Λ against electron temperature in the simulated interaction-region plasma (Figure S12g). The cooling function is indeed monotonically decreasing across much of the range of temperatures attained in the simulations, which is a necessary condition of radiative-cooling instabilities. We also calculate the cooling time at the same set of points in the simulation (Figure S12h); we find that in at least some regions in the plasma, significant cooling occurs on a time scales that is comparable to dynamical time scales (∼3 ns), which supports our claim.

TIME-RESOLVED OPTICAL THOMSON SCATTERING

Optical Thomson scattering (OTS) was used to measure the electron plasma density at TCC, where the plasma flows collided. For most shots, a frequency-tripled probe beam (351 nm light) was focused at TCC with a spot diameter of 1.2 mm and 12.8 kJ of energy delivered in a 8 ns square pulse. The scattered light was collected in a cylindrical collection volume, 1.2 mm long and 50 μm diameter, with a scattering angle of 40°. A 1,200 grooves/mm grating spectrometer was used with a spectral bandwidth of approximately 64 nm, resulting in a dispersion of 4.27 nm/mm. Calibration of the diagnostic was carried out using the 435.84 nm line from a HgAr lamp, fitted with a Gaussian instrument function of 0.291 nm.

Due to the highly turbulent plasma flow and large collection volume, we observe broad electron-plasma-wave (EPW) peaks and often multiple distinct peaks. In a uniform plasma, the EPW peak width would be dominated by Landau damping, and therefore sensitive to the electron temperature. In our experiment, however, the EPW peak width was influenced by the highly-turbulent plasma flow, and a value of the electron temperature could not reliably be determined from the OTS diagnostic. An example of the OTS data is shown in Figure S13. We see several distinct peaks at 21 ns after the start of the drive beams. The data therefore suggests that within the large collection volume, there are regions with electron density $\sim 3 \times 10^{20}$ cm^{-3} and $\sim 5 \times 10^{20}$ cm^{-3} surrounded by a broader distribution of densities.

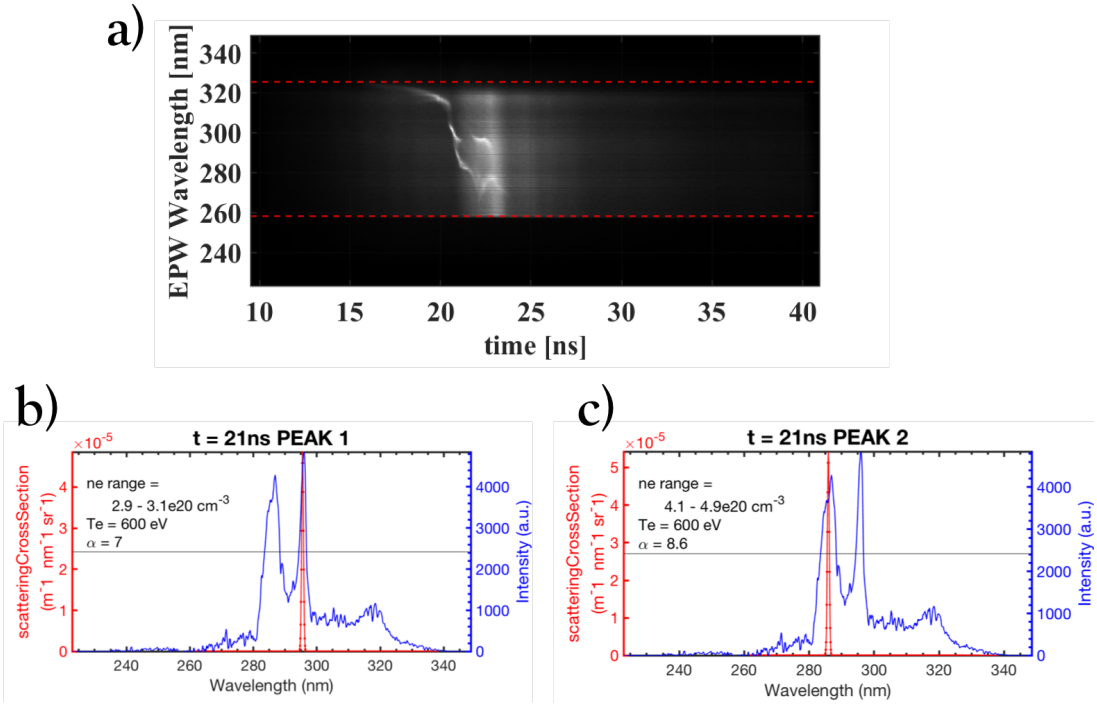

FIG. S13. **Measured Thomson scattering data. (a)** Streaked Thomson scattering EPW data for the flow collision. **(b) and (c)** Lineouts at $t = 21$ ns after the start of the drive beams. The lineouts are 10 pixel wide (226 ps). Superimposed on the data are the calculated EPW signals. Here, $\alpha = 1/k\lambda_{De}$, where k is the scattering wavenumber and λ_{De} the Debye length.

PROTON-IMAGING DIAGNOSTIC TO MEASURE MAGNETIC FIELDS

In this section, we provide further details of the analysis that we performed to measure both the root-mean-square (RMS) and maximum magnetic-field strengths attained in our experiment, as well as the field's correlation length ℓ_B.

The proton-radiography diagnostic uses a monoenergetic source of 14.7 MeV protons to backlight the plasma collision region, known to have high self-generated magnetic fields. Every proton incident upon the 10 by 10 cm CR39 detector is observed, to determine the distribution of electromagnetic fields present in the plasma. The filter pack shown in Figure S14 is composed of two 1.5 mm thick CR-39 plates to measure both the 3 MeV and 14.7 MeV protons. To achieve the proper filtering, a 25 ± 5 μm Zr was placed on the front of the pack while an Al filter was placed between both CR-39 plates. The thickness of each CR-39 plate can vary from 1.4-1.6 mm so the Al filter thickness was adjusted between $120 - 230 \pm 10$ μm to allow for 14.7 MeV protons to stop on the second CR-39 plate. The overall energy uncertainty of the system is ~ 0.34 MeV.

The proton backlighter source is a 860 μm diameter capsule, consisting of a 3.1 ± 1 μm thick SiO_2 shell filled with D_2 gas at 6 atm and ^{3}He at 12 atm, is located 18 mm from the midpoint of the two disks and ablated with 60 frequency-tripled laser beams with a 200 μm spot that deliver 43 ± 5 kJ in a 900 ps square pulse length. Previous experiments indicate the importance of driving the capsule symmetrically with high-energy beams to improve proton yield. On average, the capsule was ablated with $15 - 20$ kJ from top beams and $20 - 25$ kJ from bottom beams to allow for symmetry.

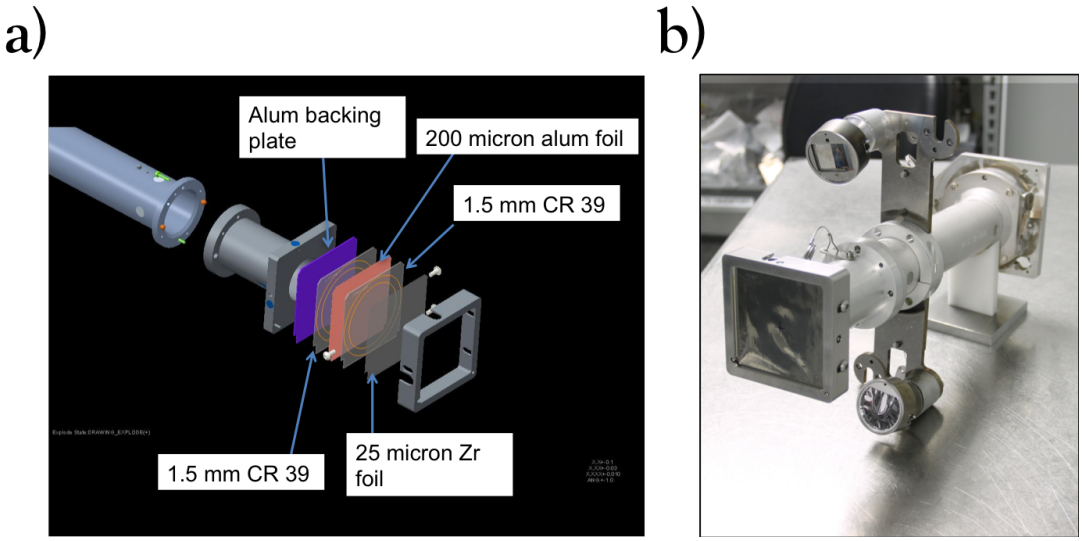

FIG. S14. **Proton radiography (PRAD) diagnostic.** **(a)** Diagram of the filter arrangement. **(b)** Photograph of the PRAD diagnostic snout.

Analysis of experimental data

As discussed in the Materials and Methods, the measurement of the magnetic field was performed by placing a 324 μm wide slit between the capsule and the colliding plasma region. Figure S15a shows the outline of the slit onto the CR-39 plate. Protons crossing the interaction region undisturbed (i.e., in the absence of any plasma or fields) should end up on the CR-39 plate only within the slit outline. By analyzing the deviations of the proton paths from their undisturbed trajectories, we can determine the mean, root-mean-square (RMS), and maximum value of the component of the path-integrated magnetic field that is co-aligned with the slit orientation (the length of the slit, or the 'axial' component). Below, we explain our approach in greater detail.

Our approach is based on the fact that in a point-projection proton-imaging set-up such as that employed on our experiment, it can be shown (in the small-deflections limit) that the position $\boldsymbol{x}_{\perp s}$ of a proton arriving on the detector is related to its initial position $\boldsymbol{x}_{\perp 0}$ prior to passing through the plasma's magnetic field $\boldsymbol{B}$ via

$$\boldsymbol{x}_{\perp s} = \mathcal{M}\boldsymbol{x}_{\perp 0} + \frac{e r_s}{m_p c V_0}\hat{\boldsymbol{n}} \times \int_0^{\ell_n} \mathrm{d}s\, \boldsymbol{B}[\boldsymbol{x}_0(s)] \,, \tag{3}$$

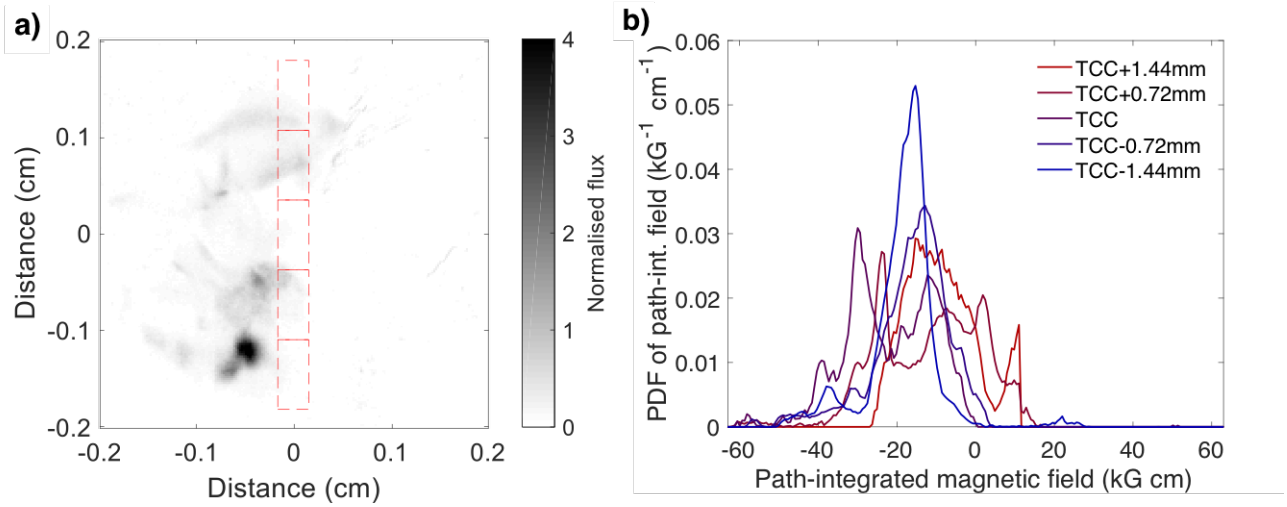

FIG. S15. **Analysis of PRAD data and magnetic field estimates. (a)** 15.0 MeV proton image recorded at $t = 25$ ns after the start of the laser drive, rotated so that the direction parallel to the slit is vertical. The normalization of the proton image is calculated relative to the mean flux of protons passing through the slit aperture that would have been measured in the absence of any magnetic fields. The imaging set-up has a $\times 19$ magnification; for clarity's sake, we remove this factor, meaning that all lengths can be compared directly to the plasma's scale. **(b)** Predicted distribution of the axial path-integrated fields at five distinct spatial locations along the slit. Here, the target chamber center (TCC) coincides with the geometric center of our target, and so with the center of the interaction region.

where $\mathcal{M}$ is the magnification of the imaging set-up, e the elementary charge, r_s the distance from the plasma to the detector, m_p the proton mass, c the speed of light, V_0 the initial proton velocity, $\hat{\boldsymbol{n}}$ the initial direction of the proton beam, ℓ_n the plasma's scale length, s the path length of the proton through the plasma, and $\boldsymbol{x}_0(s)$ the trajectory of a proton with position $\boldsymbol{x}_{\perp 0}$ through the plasma in the absence of any fields. It follows that if the projected position $\mathcal{M}\boldsymbol{x}_{\perp 0}$ of a given proton in the absence of magnetic fields is known, two components of the path-integrated magnetic field can be calculated by rearranging (3):

$$\int_0^{\ell_n} \mathrm{d}s\, \boldsymbol{B}_\perp[\boldsymbol{x}_0(s)] = -\frac{m_p c V_0}{e r_s} \hat{\boldsymbol{n}} \times [\boldsymbol{x}_{\perp s} - \mathcal{M}\boldsymbol{x}_{\perp 0}] \,, \tag{4}$$

where $\boldsymbol{B}_\perp \equiv \boldsymbol{B} - (\boldsymbol{B}_\perp \cdot \hat{\boldsymbol{n}})\hat{\boldsymbol{n}}$ are the components of $\boldsymbol{B}$ perpendicular to $\hat{\boldsymbol{n}}$. A corollary of this result is that if the initial proton beam has a finite extent, the resulting distribution of protons is related directly to the distribution of (two components of) the path-integrated magnetic field.

We apply this result to the slit-aperture proton-imaging data shown in Figure S15a. The initial position with respect to the direction perpendicular to the slit orientation of imaging protons is well constrained (i.e., on the central projected axis of the slit, with a $\pm 171\,\mu$m uncertainty arising from the slit's finite width), because any protons on the detector in the central location must have passed through the slit aperture prior to entering the plasma. Lineouts of the proton-flux distribution in the direction perpendicular to the slit orientation are therefore related to the distribution of the axial component of the magnetic field experienced by protons passing through the slit. The initial and final position with respect to the direction parallel to the slit orientation of imaging protons are not as strongly constrained, leading to an uncertainty in the position along the slit of where deflections have been acquired; we revisit the implications of this uncertainty later in this subsection.

To elucidate further the structure of the magnetic field contained in the plasma, we divide the projection of the slit aperture into five equally sized regions, with the central position of a given region separated from adjacent regions by a distance $\ell_{\mathrm{reg}} = 0.72\,\mathrm{cm}$ (see Figure S15a). We then calculate the one-dimensional distributions of protons in the direction perpendicular to the slit orientation, averaged over the region's other dimension. The resulting distributions can be converted to distributions of the axial path-integrated magnetic field in those five distinct regions. More specifically, using equation (4) and the known parameters of our imaging set-up ($V_0 = 5.3 \times 10^9\,\mathrm{cm/s}$, $\mathcal{M} \approx 19$, and $r_s = 28.2\,\mathrm{cm}$), a shift in proton position $\Delta\tilde{x} = |\boldsymbol{x}_{\perp s}/\mathcal{M} - \boldsymbol{x}_{\perp 0}|$ from its initial position (disregarding the magnification) is related to the path-integrated axial magnetic field via

$$\int_0^{\ell_n} \mathrm{d}s\, B_\parallel = 22 \left(\frac{\mathcal{M}}{19}\right) \left(\frac{V_0}{5.3 \times 10^9\,\mathrm{cm/s}}\right) \left(\frac{r_s}{28.2\,\mathrm{cm}}\right)^{-1} \left(\frac{\Delta\tilde{x}}{0.6\,\mathrm{cm}}\right) \mathrm{kG\,cm}. \tag{5}$$

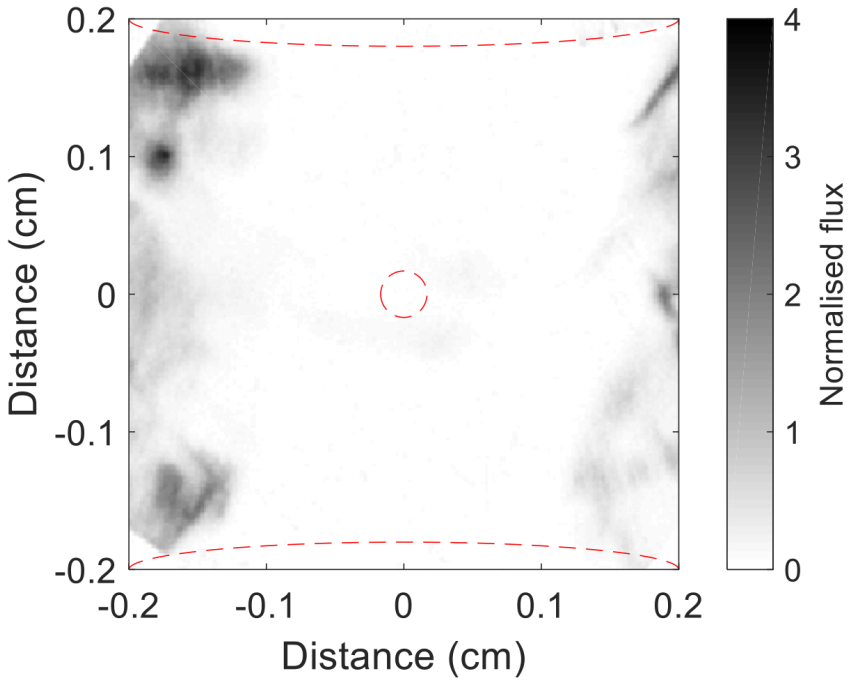

FIG. S16. **PRAD data from pinhole.** 15.0 MeV proton image of the colliding plasma jets, but with all protons except those passing through a 300 μm pinhole blocked by a Cu shield. The outline of the pinhole (as well as the projected positions of the grids) are depicted by red dashed lines. The normalization of the proton image is calculated using the mean flux of protons passing through the pinhole that would have been measured in the absence of any magnetic fields. The fusion capsule that generated the proton beam in this case was imploded 25 ns after the initiation of the main laser drive.

The distributions of the axial path-integrated fields recovered for the five regions are shown in Figure S15b. Finally, the mean, RMS, and maximum value of the axial component of the path-integrated magnetic field are calculated directly from its distribution function.

We now reconsider the consequences of the uncertainty in the initial position along the slit of any given imaging proton. Both additional experimental data (see below) and the FLASH simulations of our experiment suggest that the magnetic fields in the interaction region are statistically isotropic. We therefore assume that the uncertainty in position is comparable to the RMS magnitude of $\Delta\tilde{x}$. This in turn can be used to provide a lower bound on the minimum separation $\ell_{\rm reg}$ that can reasonably be employed when determining the path-integrated axial magnetic field at spatial locations along the slit: $\ell_{\rm reg} \geq 0.6\,{\rm cm}$. This is indeed smaller than our chosen distance between the five adjacent regions selected along the slit.

Under the assumption of isotropic magnetic fields (and assuming that the correlation length ℓ_B and spatial extent ℓ_n of those fields is known), we can relate the RMS of the axial component of the path-integrated magnetic field to the RMS of the magnetic field itself. More specifically, it can be shown that

$$\left(\int_0^{\ell_n} {\rm d}s\, B_\parallel\right)^2_{\rm RMS} = \frac{1}{2} B^2_{\rm RMS} \ell_B \ell_n \,. \tag{6}$$

Equation (6) is used in the main text to determine $B_{\rm RMS}$, assuming $\ell_n \approx 0.2\,{\rm cm}$ (a value derived from the spatial extent of the plasma seen in the X-ray images), and $\ell_B \approx 0.01\,{\rm cm}$. The lower bound on the maximum magnetic field $B_{\rm max}$ is established by noting that the kurtosis of the path-integrated axial magnetic field is always smaller than the kurtosis of the field itself, and so

$$B_{\rm max} \geq B_{\rm RMS} \frac{\left(\int_0^{\ell_n} {\rm d}s\, B_\parallel\right)_{\rm max}}{\left(\int_0^{\ell_n} {\rm d}s\, B_\parallel\right)_{\rm RMS}} \,. \tag{7}$$

The maximum displacement $\Delta\tilde{x}$ of protons is found to be $\Delta\tilde{x} \approx 2\,{\rm cm}$, which in turn gives $(\int_0^{\ell_n} {\rm d}s\, B_\parallel)_{\rm max} \approx 70\,{\rm kG\,cm}$. Equation (7) then gives the lower bound claimed in the main text.

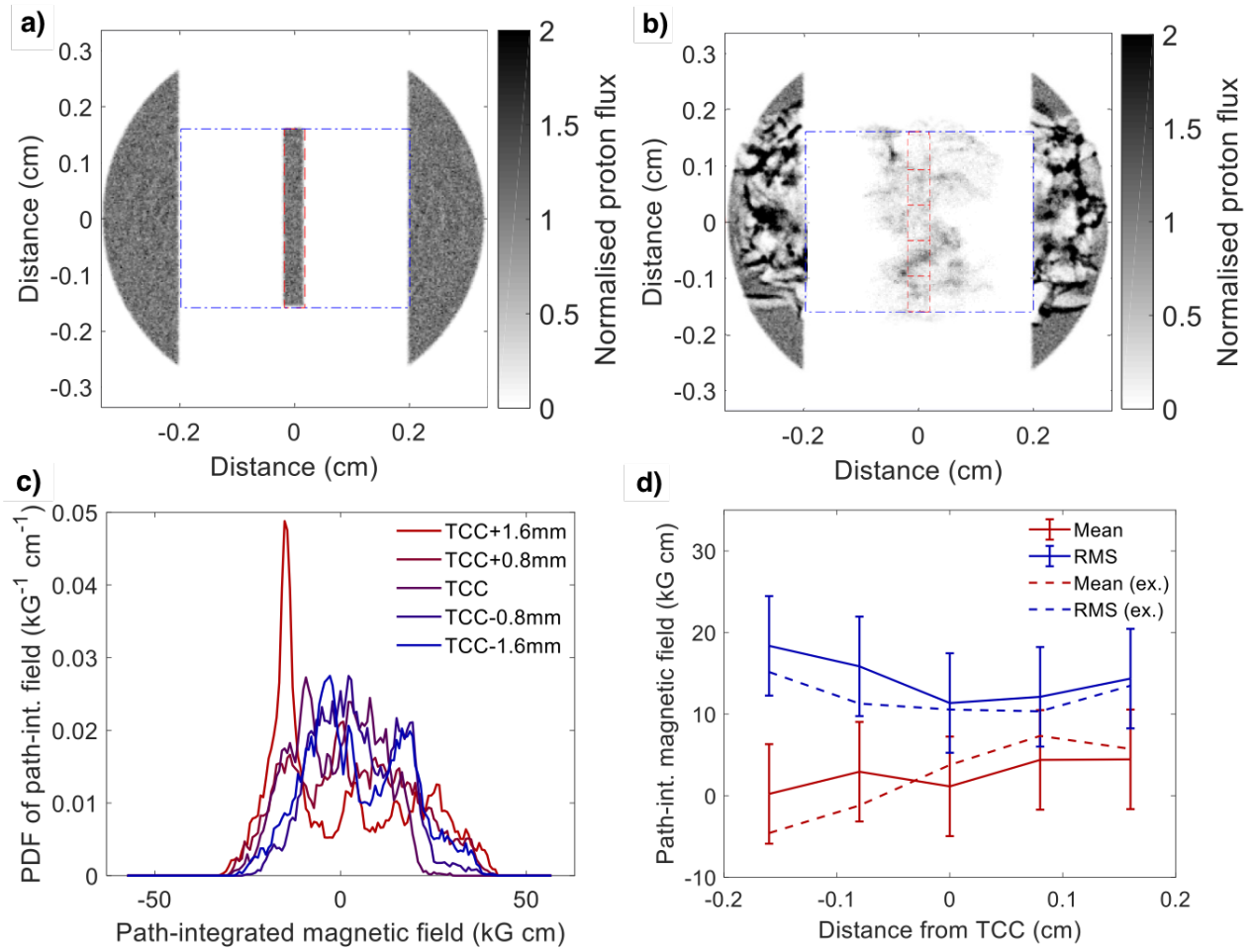

FIG. S17. **Testing the efficacy of the slit-aperture technique using the FLASH simulations. (a)** Initial proton-flux distribution introduced into proton-radiography module in FLASH simulations, in order to replicate effect of slit aperture on the proton beam. In the absence of any magnetic fields, the resulting proton image would reproduce this proton-flux distribution. The normalization of the proton-flux distribution is calculated using the mean proton flux over regions in which protons are not blocked by the shield. **(b)** Proton-flux distribution resulting from propagating the initial proton-flux distribution shown in a) through the simulated magnetic fields arising from the FLASH simulations of the NIF experiment. The normalization for the proton-flux distribution is the same as a). **(c)** Predicted distributions of the FLASH-simulated axial path-integrated fields at five distinct spatial locations along the slit. **(d)** Predicted RMS and mean axial magnetic-field strengths at five spatial locations along the slit calculated from the distributions shown in c), along with the exact results calculated directly from the FLASH-simulated path-integrated axial field.

An experimental test of the isotropic-field assumption – as well as a validation of the results derived from the slit aperture – was provided using a pinhole aperture to block the proton beam everywhere except for protons passing through the center of the interaction region (see Figure S16). In this set-up, the projected position of the beam in the absence of fields is clear (centered at the middle of the detector, with a $\sim$150 μm uncertainty in all directions), and thus Equation (4) can be used to derive the distribution of both the axial and perpendicular components of the path-integrated magnetic field. Qualitatively, we see that protons are indeed deflected in two dimensions, with displacements of similar magnitudes for both components.

Testing our approach with FLASH-simulated magnetic fields

To validate our approach for analyzing the slit-aperture proton images described in the previous section, we simulate artificial slit-aperture proton images of the magnetic fields arising in a particular FLASH simulation (25 ns, with Spitzer heat conduction switched on). We then analyze these images in the same manner as the experimental data;

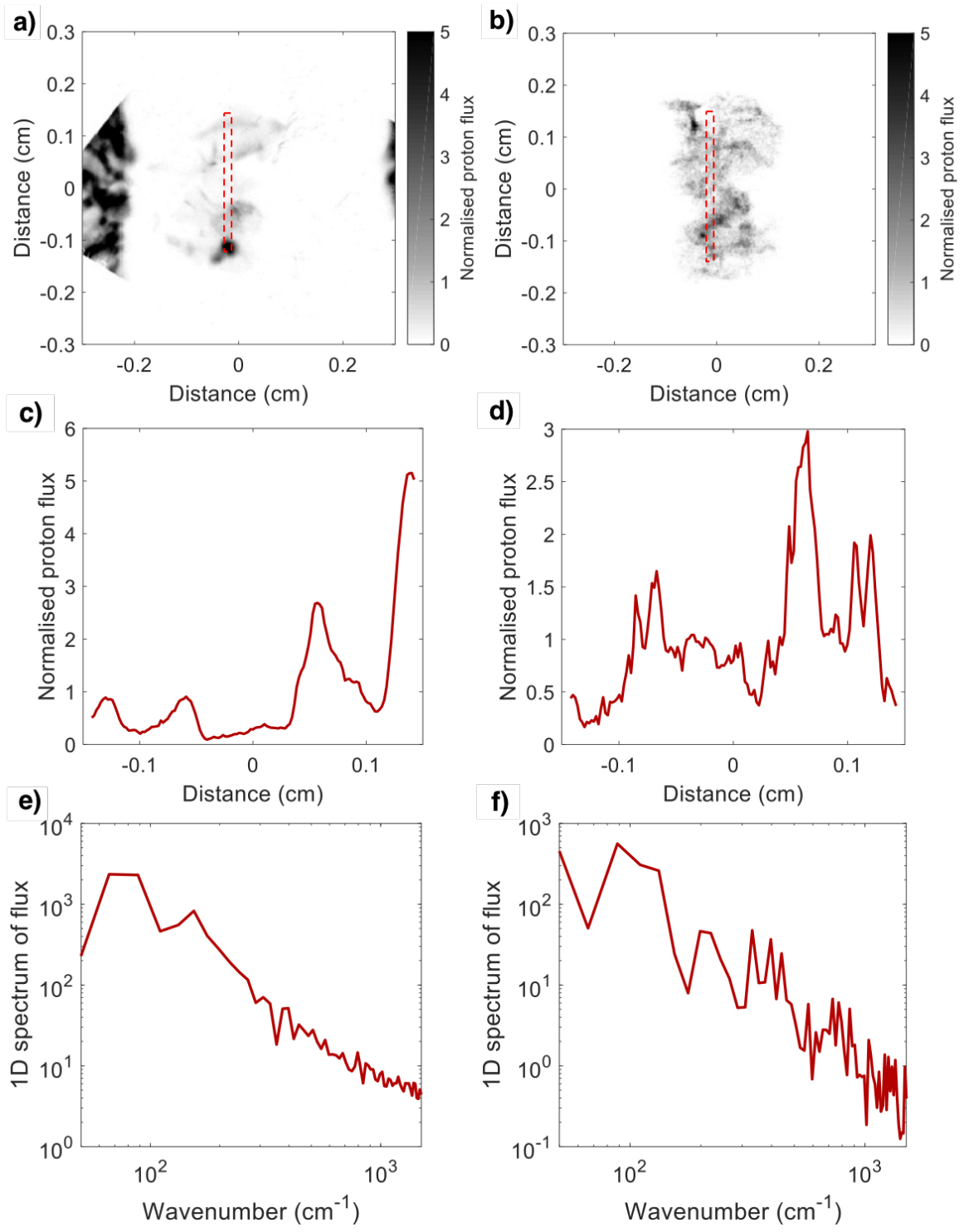

FIG. S18. **Measuring the correlation length from the scale of flux inhomogeneities in the direction parallel to the slit aperture.** **(a)** 15.0-MeV-proton image shown in Figure 3b of the main paper, rotated so that the direction parallel to the slit is vertical. The region along which averaged lineouts of the proton-flux distribution are to be taken is demarcated by a red dashed line. **(b)** Simulated 15.0-MeV-proton image (with the pre-imposed slit aperture) of the FLASH-simulated magnetic fields shown in Figure S17b. Similarly to a), the region along which averaged lineouts of the proton-flux distribution are to be taken is demarcated by a red dashed line. **(c)** Averaged lineout of the proton-flux distribution, calculated for the region indicated in a). The average is taken in the direction perpendicular to the slit orientation i.e. across the slit. **(d)** As c), but calculated using the FLASH-simulated proton image. **(e)** One-dimensional spectrum of the proton-flux calculated from the averaged lineout shown in c). **(f)** One-dimensional spectrum of the proton-flux calculated from the averaged lineout shown in d).

the resulting predicted values for the characteristic magnetic field can be compared with the true values. This analysis is presented in Figure S17.

When compared with Figure S17a, Figure S17b shows that the megagauss magnetic fields arising in the FLASH simulation lead to scattering of 15.0 MeV protons passing through the slit aperture that is qualitatively similar to that observed experimentally. As with the experimental data, we predict one-dimensional PDFs of the axial path-integrated magnetic field in five regions partitioning the length of the slit aperture (see Figure S17c) by assuming a correspondence between this quantity and one-dimensional proton-flux distributions calculated for each region by integrating the two-dimensional proton-flux distributions along their lengths. From these distributions, we then predict the RMS and mean path-integrated axial magnetic fields – and compare these predictions to the true quantities calculated directly from the FLASH-simulated fields (Figure S17d). We find agreement between these two quantities within the reported uncertainty, which is calculated in the same manner as was done for the experimental data.

Determining the correlation length of the magnetic fields

In the main text, it was claimed that the correlation length of the magnetic field in the experiment was given by $\ell_B \approx 100\,\mu$m; this claim too can be validated with the help of FLASH simulations (see Figure S18). If the characteristic deflections of protons are large enough to cause the imaging proton beam to self-intersect before reaching the detector, then the characteristic scale of any inhomogeneities in the proton-flux distribution diverges from the stochastic fields resulting in those inhomogeneities. However, in the FLASH simulations, we can compare the correlation length $\ell_{\Psi,\mathrm{FLASH}}$ of inhomogeneities in the simulated slit-aperture proton-flux distribution with the correlation length $\ell_{B,\mathrm{FLASH}}$ of the magnetic field directly; this allows an estimate to be derived for ℓ_B obtained in the actual experiment from ℓ_Ψ measured experimentally via $\ell_B \approx \ell_\Psi \ell_{B,\mathrm{FLASH}}/\ell_{\Psi,\mathrm{FLASH}}$ (viz., assuming that the ratios ℓ_B/ℓ_Ψ and $\ell_{B,\mathrm{FLASH}}/\ell_{\Psi,\mathrm{FLASH}}$ are the same, though *not* necessarily that $\ell_B \approx \ell_{B,\mathrm{FLASH}}$).

We determine ℓ_Ψ and $\ell_{\Psi,\mathrm{FLASH}}$ as follows. We take lineouts along the direction parallel to the slit aperture; the regions used to calculate these lineouts for the experimental and FLASH-simulated data are depicted in Figures S18a and S18b, respectively, and the lineouts themselves in Figures S18c and S18d. We then determine the one-dimensional spectrum $E_\Psi(k)$ of each lineout (see Figures S18e and S18f). Finally, we then calculate the correlation length using the relation

$$\ell_\Psi = \frac{1}{4\delta\Psi_{\mathrm{rms}}^2}\int_0^\infty \mathrm{d}k\,\frac{E_\Psi(k)}{k}\,. \tag{8}$$

We find that $\ell_\Psi \approx \ell_{\Psi,\mathrm{FLASH}} \approx 300\,\mu$m. We conclude that ℓ_B is likely similar to $\ell_{B,\mathrm{FLASH}}$. In the case of the FLASH simulations, the correlation length can be calculated directly, and is found to be $\ell_{B,\mathrm{FLASH}} \approx 100\,\mu$m inside the interaction region. We therefore use this value for the experiment.

We note that related experiments on the Omega laser have directly measured values of ℓ_B whose ratio with respect to the outer scale L of the turbulent cascade is (up to) $\sim$50% larger than observed here ($\ell_B \approx L/4$) [20]. However, we do not believe that these results are inconsistent with those presented in this paper, because it was also shown in [20] that the technique with which the correlation length was measured can manifest systematic biases towards larger values of up to a similar ($\sim$50%) magnitude as the discrepancy between the Omega and NIF values of ℓ_B. Furthermore, the uncertainty on the reported RMS magnetic-field strength B_{RMS} due to a $\sim$50% uncertainty on ℓ_B is only $\sim$25%; this uncertainty does not therefore affect any of our main qualitative conclusions. We also observe that FLASH simulations of the experiments on the Omega Laser Facility gave notably smaller correlation lengths ($\ell_{B,\mathrm{FLASH}} \approx L/10$) than the experimental data (in spite of modelling the hydrodynamics accurately), and also smaller values of ℓ_Ψ than we attained experimentally. There were several possible explanations that were put forward to explain the discrepancy seen in Ref. [20]; because the physical processes underpinning these explanations are also present in the NIF experiment, it remains an open question as to why exactly the FLASH simulations of the NIF experiment seem to give a similar correlation length to that attained experimentally, but the simulations of the Omega experiment do not. We will explore this question in future work.

REFERENCES AND NOTES

1. E. G. Zweibel, C. Heiles, Magnetic fields in galaxies and beyond. *Nature* **385**, 131–136 (1997).

2. V. Vacca, M. Murgia, F. Govoni, T. Enßlin, N. Oppermann, L. Feretti, G. Giovannini, F. Loi Magnetic fields in galaxy clusters and in the large-scale structure of the Universe. *Galaxies* **6**, 142 (2018).

3. L. L. Cowie, J. Binney, Radiative regulation of gas flow within clusters of galaxies - A model for cluster x-ray sources. *Astrophys. J.* **215**, 723 (1977).

4. A. C. Fabian, Cooling flows in clusters of galaxies. *Annu. Rev. Astron. Astrophys.* **32**, 277–318 (1994).

5. A. Fabian, Observational evidence of active galactic nuclei feedback. *Annu. Rev. Astron. Astrophys.* **50**, 455–489 (2012).

6. L. Bîrzan, D. A. Rafferty, P. E. J. Nulsen, B. R. McNamara, H. J. A. Rottgering, M. W. Wise, R. Mittal, The duty cycle of radio-mode feedback in complete samples of clusters. *Mon. Not. R. Astron. Soc.* **427**, 3468–3488 (2012).

7. E. Churazov, W. Forman, C. Jones, H. Böhringer, Asymmetric, arc minute scale structures around NGC 1275. *Astron. Astrophys.* **356**, 788 (2000).

8. R. Narayan, M. V. Medvedev, Thermal conduction in clusters of Galaxies. *Astrophys. J.* **562**, L129–L132 (2001).

9. M. Ruszkowski, M. C. Begelman, Heating, conduction and minimum temperatures in cooling flows. *Astrophys. J.* **581**, 223–228 (2002).

10. M. W. Kunz, A. A. Schekochihin, S. C. Cowley, J. J. Binney, J. S. Sanders, Thermally stable heating mechanism for the intracluster medium: Turbulence, magnetic fields and plasma instabilities. *Mon. Not. R. Astron. Soc.* **410**, 2446–2457 (2011).

11. M. Markevitch, A. Vikhlinin, Shocks and cold fronts in galaxy clusters. *Phys. Rep.* **443**, 1–53 (2007).

12. S. V. Komarov, E. M. Churazov, M. W. Kunz, A. A. Schekochihin Thermal conduction in a mirror-unstable plasma. *Mon. Not. R. Astron. Soc.* **460**, 467–477 (2016).

13. S. V. Komarov, E. M. Churazov, A. A. Schekochihin, J. A. ZuHone Suppression of local heat flux in a turbulent magnetized intracluster medium. *Mon. Not. R. Astron. Soc.* **440**, 1153–1164 (2014).

14. S. Komarov, A. A. Schekochihin, E. Churazov, A. Spitkovsky Self-inhibiting thermal conduction in a high-β, whistler-unstable plasma. *J. Plasma Phys.* **84**, 905840305 (2018).

15. G. T. Roberg-Clark, J. F. Drake, C. S. Reynolds, M. Swisdak Suppression of electron thermal conduction by whistler turbulence in a sustained thermal gradient. *Phys. Rev. Lett.* **120**, 035101 (2018).

16. J. A. ZuHone, M. Markevitch, M. Ruszkowski, D. Lee, Cold fronts and gas sloshing in galaxy clusters with anisotropic thermal conduction. *Astrophys. J.* **762**, 69 (2013).

17. B. Smith, B. W. O'Shea, G. M. Voit, D. Ventimiglia, S. W. Skillman Cosmological simulations of isotropic conduction in galaxy clusters. *Astrophys. J.* **778**, 152 (2013).

18. G. Gregori, B. Reville, F. Miniati, The generation and amplification of intergalactic magnetic fields in analogue laboratory experiments with high power lasers. *Phys. Rep.* **601**, 1–34 (2015).

19. P. Tzeferacos, A. Rigby, A. F. A. Bott, A. R. Bell, R. Bingham, A. Casner, F. Cattaneo, E. M. Churazov, J. Emig, F. Fiuza, C. B. Forest, J. Foster, C. Graziani, J. Katz, M. Koenig, C. K. Li, J. Meinecke, R. Petrasso, H. S. Park, B. A. Remington, J. S. Ross, D. Ryu, D. Ryutov, T. G. White, B. Reville, F. Miniati, A. A. Schekochihin, D. Q. Lamb, D. H. Froula, G. Gregori Laboratory evidence of dynamo amplification of magnetic fields in a turbulent plasma. *Nat. Commun.* **9**, 591 (2018).

20. A. F. A. Bott, P. Tzeferacos, L. Chen, C. A. J. Palmer, A. Rigby, A. R. Bell, R. Bingham, A. Birkel, C. Graziani, D. H. Froula, J. Katz, M. Koenig, M. W. Kunz, C. Li, J. Meinecke, F. Miniati, R. Petrasso, H. S. Park, B. A. Remington, B. Reville, J. S. Ross, D. Ryu, D. Ryutov, F. H. Séguin, T. G.

White, A. A. Schekochihin, D. Q. Lamb, G. Gregori Time-resolved turbulent dynamo in a laser plasma. *Proc. Natl. Acad. Sci.* **118**, e2015729118 (2021).

21. P. Tzeferacos, A. Rigby, A. Bott, A. R. Bell, R. Bingham, A. Casner, F. Cattaneo, E. M. Churazov, J. Emig, N. Flocke, F. Fiuza, C. B. Forest, J. Foster, C. Graziani, J. Katz, M. Koenig, C. K. Li, J. Meinecke, R. Petrasso, H. S. Park, B. A. Remington, J. S. Ross, D. Ryu, D. Ryutov, K. Weide, T. G. White, B. Reville, F. Miniati, A. A. Schekochihin, D. H. Froula, G. Gregori, D. Q. Lamb Numerical modeling of laser-driven experiments aiming to demonstrate magnetic field amplification via turbulent dynamo. *Phys. Plasmas* **24**, 041404 (2017).

22. E. Churazov, P. Arevalo, W. Forman, C. Jones, A. Schekochihin, A. Vikhlinin, I. Zhuravleva Arithmetic with x-ray images of galaxy clusters: Effective equation of state for small-scale perturbations in the ICM. *Mon. Not. R. Astron. Soc.* **463**, 1057–1067 (2016).

23. A. R. Bell, R. G. Evans, D. J. Nicholas Elecron energy transport in steep temperature gradients in laser-produced plasmas. *Phys. Rev. Lett.* **46**, 243–246 (1981).

24. G. Gregori, S. H. Glenzer, J. Knight, C. Niemann, D. Price, D. H. Froula, M. J. Edwards, R. P. J. Town, A. Brantov, W. Rozmus, V. Y. Bychenkov, Effect of nonlocal transport on heat-wave propagation. *Phys. Rev. Lett.* **92**, 205006 (2004).

25. M. Markevitch, P. Mazzotta, A. Vikhlinin, D. Burke, Y. Butt, L. David, H. Donnelly, W. R. Forman, D. Harris, D. W. Kim, S. Virani, J. Vrtilek [ITAL]Chandra[/ITAL] temperature map of A754 and constraints on thermal conduction. *Astrophys. J.* **586**, L19–L23 (2003).

26. D. A. Tidman, R. A. Shanny, Field-generating thermal instability in laser-heated plasmas. *Phys. Fluids* **17**, 1207 (1974).

27. M. G. Haines, Thermal instability and magnetic field generated by large heat flow in a plasma, especially under laser-fusion conditions. *Phys. Rev. Lett.* **47**, 917–920 (1981).

28. D. E. Evans, J. Katzenstein, Laser light scattering in laboratory plasmas. *Rep. Prog. Phys.* **32**, 207–271 (1969).

29. H. A. Rose, D. F. DuBois, Laser hot spots and the breakdown of linear instability theory with application to stimulated Brillouin scattering. *Phys. Rev. Lett.* **72**, 2883–2886 (1994).

30. A. Bott, C. Graziani, P. Tzeferacos, T. G. White, D. Q. Lamb, G. Gregori, A. A. Schekochihin, Proton imaging of stochastic magnetic fields. *J. Plasma Phys.* **83**, 905830614 (2017).

31. G. A. Rochau, J. E. Bailey, G. A. Chandler, T. J. Nash, D. S. Nielsen, G. S. Dunham, O. F. Garcia, N. R. Joseph, J. W. Keister, M. J. Madlener, D. B. Morgan, K. J. Moy, M. Wu, Energy dependent sensitivity of microchannel plate detectors. *Rev. Sci. Instrum.* **77**, 10E323 (2006).

32. B. A. Fryxell, K. Olson, P. Ricker, F. X. Timmes, M. Zingale, D. Q. Lamb, P. Mac Neice, R. Rosner, J. W. Truran, H. Tufo, FLASH: An adaptive mesh hydrodynamics code for modeling astrophysical thermonuclear flashes. *Astrophys. J. Suppl.* **131**, 273–334 (2000).

33. D. Lee, A solution accurate, efficient and stable unsplit staggered mesh scheme for three dimensional magnetohydrodynamics. *J. Comput. Phys.* **243**, 269–292 (2013).

34. P. Tzeferacos, M. Fatenejad, N. Flocke, C. Graziani, G. Gregori, D. Q. Lamb, D. Lee, J. Meinecke, A. Scopatz, K. Weide, FLASH MHD simulations of experiments that study shock-generated magnetic fields. *High Energ. Dens. Phys.* **17**, 24–31 (2015).

35. S. I. Braginskii, Transport processes in a plasma. *Rev. Plasma Phys.* **1**, 205 (1965).

36. M. Fatenejad, B. Fryxell, J. Wohlbier, E. Myra, D. Lamb, C. Fryer, C. Graziani Collaborative comparison of simulation codes for high-energy-density physics applications. *High Energ. Dens. Phys.* **9**, 63–66 (2013).

37. C. Orban, M. Fatenejad, S. Chawla, S. C. Wilks, D. Q. Lamb, A radiation-hydrodynamics code comparison for laser-produced plasmas: FLASH versus HYDRA and the results of validation experiments (2013); arXiv preprint arXiv:1306.1584.

38. J. Meinecke, H. W. Doyle, F. Miniati, A. R. Bell, R. Bingham, R. Crowston, R. P. Drake, M. Fatenejad, M. Koenig, Y. Kuramitsu, C. C. Kuranz, D. Q. Lamb, D. Lee, M. J. MacDonald, C. D. Murphy, H. S. Park, A. Pelka, A. Ravasio, Y. Sakawa, A. A. Schekochihin, A. Scopatz, P.

Tzeferacos, W. C. Wan, N. C. Woolsey, R. Yurchak, B. Reville, G. Gregori Turbulent amplification of magnetic fields in laboratory laser-produced shock waves. *Nat. Phys.* **10**, 520–524 (2014).

39. K. Falk, E. J. Gamboa, G. Kagan, D. S. Montgomery, B. Srinivasan, P. Tzeferacos, J. F. Benage Equation of state measurements of warm dense carbon using laser-driven shock and release technique. *Phys. Rev. Lett.* **112**, 155003 (2014).

40. R. Yurchak, A. Ravasio, A. Pelka, S. Pikuz, E. Falize, T. Vinci, M. Koenig, B. Loupias, A. Benuzzi-Mounaix, M. Fatenejad, P. Tzeferacos, D. Q. Lamb, E. G. Blackman Experimental demonstration of an inertial collimation mechanism in nested outflows. *Phys. Rev. Lett.* **112**, 155001 (2014).

41. C. K. Li, P. Tzeferacos, D. Lamb, G. Gregori, P. A. Norreys, M. J. Rosenberg, R. K. Follett, D. H. Froula, M. Koenig, F. H. Seguin, J. A. Frenje, H. G. Rinderknecht, H. Sio, A. B. Zylstra, R. D. Petrasso, P. A. Amendt, H. S. Park, B. A. Remington, D. D. Ryutov, S. C. Wilks, R. Betti, A. Frank, S. X. Hu, T. C. Sangster, P. Hartigan, R. P. Drake, C. C. Kuranz, S. V. Lebedev, N. C. Woolsey, Scaled laboratory experiments explain the kink behaviour of the crab nebula jet. *Nat. Commun.* **7**, 13081 (2016).

42. A. Rigby, F. Cruz, B. Albertazzi, R. Bamford, A. R. Bell, J. E. Cross, F. Fraschetti, P. Graham, Y. Hara, P. M. Kozlowski, Y. Kuramitsu, D. Q. Lamb, S. Lebedev, J. R. Marques, F. Miniati, T. Morita, M. Oliver, B. Reville, Y. Sakawa, S. Sarkar, C. Spindloe, R. Trines, P. Tzeferacos, L. O. Silva, R. Bingham, M. Koenig, G. Gregori Electron acceleration by wave turbulence in a magnetized plasma. *Nat. Phys.* **14**, 475–479 (2018).

43. Y. Lu, P. Tzeferacos, E. Liang, R. K. Follett, L. Gao, A. Birkel, D. H. Froula, W. Fu, H. Ji, D. Lamb, C. K. Li, H. Sio, R. Petrasso, M. S. Wei Numerical simulation of magnetized jet creation using a hollow ring of laser beams. *Phys. Plasmas* **26**, 022902 (2019).

44. L. Gao, E. Liang, Y. Lu, R. K. Follet, H. Sio, P. Tzeferacos, D. H. Froula, A. Birkel, C. K. Li, D. Lamb, R. Petrasso, W. Fu, M. Wei, H. Ji Mega-gauss plasma jet creation using a ring of laser beams. *Astrophys. J.* **873**, L11 (2019).

45. T. G. White, M. T. Oliver, P. Mabey, M. Kühn-Kauffeldt, A. F. A. Bott, L. N. K. Döhl, A. R. Bell, R. Bingham, R. Clarke, J. Foster, G. Giacinti, P. Graham, R. Heathcote, M. Koenig, Y. Kuramitsu, D. Q. Lamb, J. Meinecke, T. Michel, F. Miniati, M. Notley, B. Reville, D. Ryu, S. Sarkar, Y. Sakawa, M. P. Selwood, J. Squire, R. H. H. Scott, P. Tzeferacos, N. Woolsey, A. A. Schekochihin, G. Gregori, Supersonic plasma turbulence in the laboratory. *Nat. Commun.* **10**, 1758 (2019).

46. L. E. Chen, A. F. A. Bott, P. Tzeferacos, A. Rigby, A. Bell, R. Bingham, C. Graziani, J. Katz, M. Koenig, C. K. Li, R. Petrasso, H. S. Park, J. S. Ross, D. Ryu, T. G. White, B. Reville, J. Matthews, J. Meinecke, F. Miniati, E. G. Zweibel, S. Sarkar, A. A. Schekochihin, D. Q. Lamb, D. H. Froula, G. Gregori Transport of high-energy charged particles through spatially intermittent turbulent magnetic fields. *Astrophys. J.* **892**, 114 (2020).

47. A. F. A. Bott, L. Chen, G. Boutoux, T. Caillaud, A. Duval, M. Koenig, B. Khiar, I. Lantuéjoul, L. le-Deroff, B. Reville, R. Rosch, D. Ryu, C. Spindloe, B. Vauzour, B. Villette, A. A. Schekochihin, D. Q. Lamb, P. Tzeferacos, G. Gregori, A. Casner Inefficient magnetic-field amplification in supersonic laser-plasma turbulence. *Phys. Rev. Lett.* **127**, 175002 (2021).

48. S. A. Muller, D. N. Kaczala, H. M. Abu-Shawareb, E. L. Alfonso, L. C. Carlson, M. Mauldin, P. Fitzsimmons, D. Lamb, P. Tzeferacos, L. Chen, G. Gregori, A. Rigby, A. Bott, T. G. White, D. Froula, J. Katz Evolution of the design and fabrication of astrophysics targets for turbulent dynamo (tdyno) experiments on omega. *Fusion Sci. Technol.* **73**, 434–445 (2018).

49. P. Colella, P. R. Woodward, The piecewise parabolic method (ppm) for gas-dynamical simulations. *J. Comput. Phys.* **54**, 174–201 (1984).